From: THE GEOPHYSICS OF SEA ICE
Edited by Norbert Untersteiner
(Plenum Publishing Corporation, 1986)

CHAPTER 4

THE UPPER OCEAN

Miles G. McPhee

McPhee Research Company
Yakima, Washington

1. INTRODUCTION

Since the drift of the Fram nearly ninety years ago, it has been recognized that turbulent exchange in the upper ocean is a major factor in the dynamic and thermodynamic regime of high-latitude, ice-covered seas. Ekman (1905) credited the inspiration for his theory of wind drift currents, which was to become a cornerstone of physical oceanography and meteorology, to Nansen's qualitative description of the effect of the earth's rotation on the upper layers of the ocean, which he deduced from his observations that Fram drifted consistently 20-40 degrees right of the surface wind. They were among the first to appreciate the unique observational platform provided by pack ice.

Experiments performed in polar regions over the past decade or so have provided significant additions to our knowledge of how the upper ocean works, and in many ways it is an exciting time to be studying the ice-ocean boundary. Our aim in this work is to review these findings, and to place them in the framework of a boundary-layer theory which, despite its relative simplicity, turns out to be surprisingly comprehensive. We start by pointing out some basic features, illustrating them with experimental data taken mainly from the AIDJEX studies. We then review and develop theoretical descriptions for momentum transfer in the boundary layer, which leads to consideration of density structure in the upper ocean, and inclusion of the conservation equation for buoyancy (governed mainly by salinity). This provides at least a

theoretical staging point for addressing the extremely complex fluid-dynamical regime of the marginal ice zone.

2. BASICS

When a steady wind blows across the surface of an ice-covered ocean, there often develops in the ice cover a nearly steady-state balance among four forces: the surface wind traction, the gradient of internal ice stress, the Coriolis force on the ice column (assuming a fixed-to-earth reference frame), and a traction exerted by the ocean on the ice undersurface. The last force is the surface manifestation of a turbulent oceanic boundary layer (OBL) which provides the mechanism for momentum exchange between the ice and ocean. The OBL is affected by rotational (Coriolis) forces and therefore falls, along with the atmospheric boundary layer (ABL), into the general category of planetary boundary layers. We shall show that the two boundary layers are closely related in many respects, but that there are also some important and interesting differences.

Consider a force balance like that described above but idealized so that first, the internal ice force is negligible, and second, the undisturbed ocean is at rest. While the latter may seem artificial, it can approximate a real state in which the entire wind-drift system is advected by the mean geostrophic flow. Since normal geostrophic currents are at most a few percent of the surface wind, this is often a useful approximation and we shall use it repeatedly below. The force balance is diagrammed in Figure la; its relative proportions represent average observed conditions during summer at the AIDJEX camps, when internal stress gradients were small.

The sketch demonstrates that the OBL surface stress (which is the negative of the water stress shown) acts in a direction about 25° to the left of the surface velocity, $\hat{V}_o$. From this observational fact alone, we can infer much about the structure of the OBL. It helps to consider the problem from the viewpoint of an observer drifting on the ice floe, whom we imagine to be dropping a probe that measures velocity relative to the drifting ice and turbulent stress. Near the surface the kinematic stress would be about the same as $\hat{\tau}_o$, and by analogy with other constant-stress, wall-bounded turbulent flows, we would expect a region of shear with relative velocity varying logarithmically in the same direction as turbulent stress. As the probe drops, the stress would diminish and veering of both the horizontal stress vector and the mean current would be noted. At some depth stress would vanish and the observer would measure a "free-stream" current, $-\hat{V}_o$, at this and greater depths. The currents are sketched in plan view (hodograph) in Figure 1b. That part of the profile close to the ice, where the relative velocity is logarithmic and unidirectional

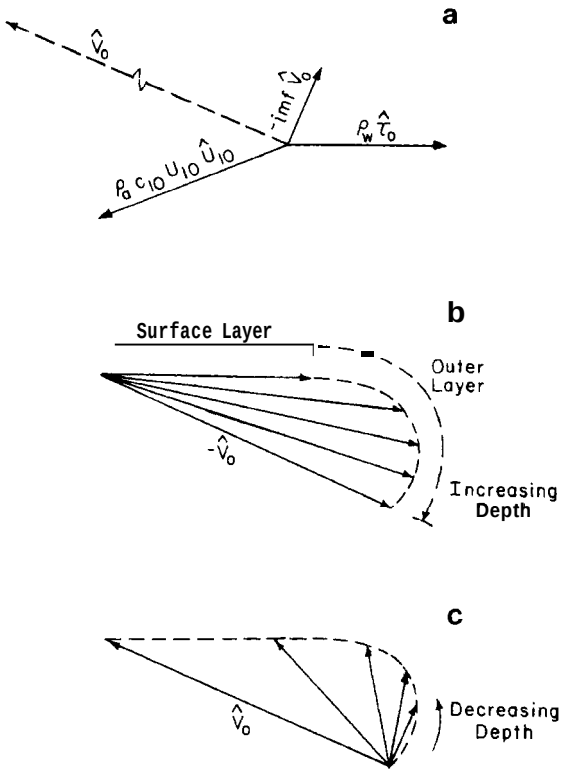

Fig. 1. Schematic of ice force balance (a), plan view of OBL velocity as viewed from drifting ice (b), velocity as viewed in frame fixed to earth (c).

is called the surface layer. The region farther from the interface, where the relative velocity veers noticeably, is called the outer, or Ekman layer. The basic structure diagrammed in Figure 1 should be studied closely, particularly the difference in currents measured in a fixed-to-earth reference frame (Figure 1c) vis-a-vis as measured in a reference iramedrifting with the ice. These two ways of viewing the OBL have an exact analog in the way that the ABL is described, either in terms of the actual wind or by the "velocity defect" (see Tennekes and Lumley, 1972, Chapter 5).

2.1 Equations

Conservation equations for turbulent flow in a horizontally homogeneous fluid may be written:

Momentum: $$\frac{\partial \underline{V}}{\partial t} + f \underset{\sim}{k} \times \underline{V} = -\frac{1}{\rho} \nabla p - g \underset{\sim}{k} - \frac{\partial}{\partial x}(\overline{w' \underline{v}'}) \qquad (4.1)$$

Heat: $$\frac{\partial \Theta}{\partial t} + \frac{\partial}{\partial z}\overline{w'\theta'} = Q_\theta/\rho c_p \qquad (4.2)$$

Salinity: $$\frac{\partial S}{\partial t} + \frac{\partial}{\partial z}\overline{w'S'} = Q_s \qquad (4.3)$$

Where $\underset{\sim}{V}$ is the "mean" horizontal velocity (in the sense that its variation is slow relative to turbulent fluctuations); f is the Coriolis parameter (twice the vertical component of the earth's angular frequency); ρ is density; p is pressure; w' is the vertical turbulent fluctuation velocity; $\underset{\sim}{v}'$ is the horizontal turbulent velocity; Θ and θ' are mean and turbulent fluctuation of temperature; Q_θ is a source term for heat in fluid with heat capacity, c_p; S and S' are mean and turbulent fluctuation of salinity; and Q_s is a source term for salinity. Reynolds averaging has been performed over time scales commensurate with a presumed spectral gap; i.e., for an arbitrary property, a, $a = A + a'$ where A is the average over a time long compared to the scale of turbulent fluctuations, but short compared to inertial and synoptic time scales.

The equation of state for seawater is approximated by

$$\frac{\rho - \rho_o}{\rho_o} = -\alpha_\theta(\theta - \theta_o) + \alpha_s(S - S_o) \qquad (4.4)$$

where ρ_o, θ_o, and S_o are reference density, temperature, and salinity.

Although the fluid is assumed horizontally homogeneous, a large-scale horizontal pressure gradient is allowed, which, through the hydrostatic relation, is identified with the gradient of the sea surface elevation, η,

$$\frac{1}{\rho}\nabla p = g\nabla\eta .$$

When no turbulence is present, eq. (4.1) defines the geostrophic velocity due to sea surface tilt

$$f\underset{\sim}{k} \times \underset{\sim}{V}_g = -g\nabla\eta . \qquad (4.5)$$

For later convenience we introduce complex notation for horizontal vectors

$$\underset{\sim}{V} = (V_x, V_y) = \hat{V} = V_x + iV_y = Ve^{i\theta_V}, \quad i = \sqrt{-1} \ .$$

When a symbol is written with a caret (^), a complex, two-dimensional vector is indicated; when the symbol is written without a caret, magnitude only is meant: i.e., $V = |\hat{V}|$. The kinematic Reynolds stress is

$$\hat{\tau} = -(\overline{u'w'} + i\,\overline{v'w'}) \quad .$$

Substituting $\hat{V}_g$ from (45) into (4.1) results in the horizontal momentum equation

$$\frac{\partial \hat{V}}{\partial t} + if(\hat{V} - \hat{V}_g) = \frac{\partial \hat{\tau}}{\partial z} \quad . \tag{4.6}$$

In the Coriolis term, multiplication by i, which represents a 90° counterclockwise rotation, replaces the k x operator. If $\hat{V}_g$ is constant over the time scale being considered, the transformation $\hat{V}' = \hat{V} - \hat{V}_g$ results in a particularly useful form of the momentum equation

$$\frac{\partial \hat{V}}{\partial t} + if\hat{V} = \frac{\partial \hat{\tau}}{\partial z}$$

where the prime is dropped and it is understood that all velocities are relative to the undisturbed, steady geostrophic flow. In what follows, this convention is observed unless otherwise stated.

2.2 Turbulence

A simple but powerful tool for describing the basic transfer mechanism in high-Reynolds-number flows is the mixing length hypothesis developed originally by Prandtl (see, e.g., Hinze, 1975). The concept is sketched in Figure 2, depicting an overturning eddy in fluid characterized by a vertical gradient of an arbitrary property, ε. To be truly turbulent, the flow must be highly diffusive, with fluid parcels caught in a turbulent eddy readily transferring their concentration of ε to the surrounding fluid in a cascade of smaller and smaller eddies. In Figure 2, Parcel 1 distributes a deficit of ε above h, Parcel 2 delivers an excess

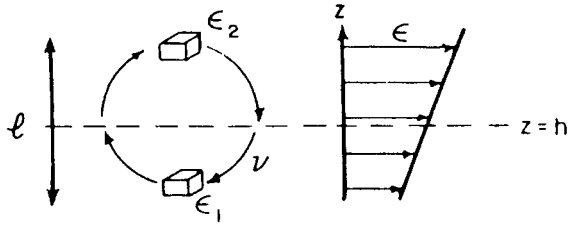

Fig. 2. Turbulent exchange in a flow with a gradient of an arbitrary property, ε.

below h, so that there is a net downward flux of ε. The magnitude of the flux apparently depends on the gradient, $\partial\varepsilon/\partial z$; the speed with which the eddy overturns, v ; and the size of the most energetic eddies found in the vicinity, ℓ_ε. The last two quantities represent scales at which the smaller eddies can keep pace with the large eddies at diffusing away variations in ε. The simplest expression for the flux, F_ε, is the product

$$F_\varepsilon = -v_\varepsilon \ell_\varepsilon \frac{\partial \varepsilon}{\partial z} \tag{4.7}$$

and by analogy with molecular transfer processes, an "eddy diffusivity" may be defined, $K_\varepsilon = v_\varepsilon \ell_\varepsilon$, which depends on the turbulent flow rather than the molecular properties of the particular fluid. This is a crucial aspect of high-Reynolds-number turbulence, and provides a basis for comparing, e.g., atmospheric and oceanic 'boundary layers.

Let ε stand for vector momentum. The momentum flux across a horizontal plane is the negative of the horizontal part of the turbulent stress tensor, and is given by

$$\hat{F}_m = -\rho_w \hat{\tau} = -\rho_w K_m \frac{\partial \hat{V}}{\partial z} \quad . \tag{4.8}$$

ε may stand for other properties, like temperature or salinity, and the same basic process is thought to apply; this is essentially Reynolds analogy. Note, however, that different properties may have different v_ε and ℓ_ε scales in the same flow, so that eddy diffusivities are not necessarily the same. Indeed, it is likely that turbulent diffusion of heat and salt occurs at different rates in the arctic thermocline (Neshyba et al., 1971).

There are obvious examples where the physics expressed by eq. (4.7) are not sophisticated enough to describe the particular flow; e.g., when flow separation occurs near a pressure ridge keel, or where there is double diffusion when a stabilizing mean salinity gradient coincides with a destabilizing temperature gradient. Rut despite its limitations, we shall show that the mixing length hypothesis can be very useful for interpreting the OBL, provided the scales are chosen carefully.

2.3 Scales

The planetary boundary layer (PBL) is often broken conceptually into a surface layer, where turbulence is affected directly by the hydraulic roughness of the solid surface, and an outer layer where the turbulence is "free" in the sense that it does not depend on the actual physical characteristics of the interface.

The idea of a surface layer arises naturally from numerous observations in the atmosphere that show under typical conditions the mean wind profile varying dramatically in the first few meters, but turbulent stress changing by only a few percent over the lower tens of meters. The wind shear in the neutrally buoyant (no density variations) surface layer has been shown to satisfy very closely the relationship

$$\frac{kz}{u_*}\frac{\partial V}{\partial z} = 1 \tag{4.9}$$

where u_* is the magnitude of the surface friction velocity, defined in vector form by $\hat{\tau}_o = u_*\hat{u}_*$, where τ_o is the kinematic interfacial stress. With stress nearly constant, eqs. (4.7) and (4.8) when combined with the empirical result eq. (4.9), imply that the turbulence scales in the surface layer are $v_m = u_*$ and $\ell_m = kz$. Integration of eq. (4.9) results in a logarithmic velocity profile relative to the surface

$$|\hat{V}(z) - \hat{V}_o| = \frac{u_*}{k} \ln \frac{|z|}{z_o} \tag{4.10}$$

The integration constant, z_o, is called the roughness length and on a surface of uniform roughness elements it corresponds in some way to the physical size of the elements. (With a surface like sea ice, punctuated by hummocks and pressure ridge keels, its meaning is more abstract as will be discussed later.) From the "law of the wall" eq. (4.10), the scales $\hat{u}_*$ for velocity and z_o for length are obvious choices for the surface layer.

Consider next the outer region of free turbulence. The steady-state form of eq. (4.6) is a balance between the Coriolis acceleration and the turbulent stress gradient.

$$if\hat{V} = \frac{\partial \hat{\tau}}{\partial z} \tag{4.11}$$

Through the outer layer the stress varies from near its surface value to zero, thus an obvious scale for stress is again the interfacial stress, $\hat{\tau}_o = u_*\hat{u}_*$.

It might be argued that the choice of $\hat{V}_o$ as the velocity scale for the outer layer is just as obvious; however, it is well to examine this in light of the assertion that the turbulence of the outer layer does not sense surface characteristics directly. The total change of velocity across the surface layer depends on z_o, and since most of the shear in the direction of surface stress occurs within the surface layer, z_o has an obvious impact on $\hat{V}_o$. But if turbulence below the surface layer does not sense z_o, then mean velocity there cannot either, and by this reasoning $\hat{V}_o$ is a

poor choice for its scale. With no other information, a good working hypothesis is that $\hat{u}$, is a better scale, because certainly turbulence in the outer layer must respond in some way to surface stress. In the absence of an externally imposed length scale (such as h_{BL}, the depth of the mixed layer above a strong density gradient), these choices of stress and velocity scales force the length scale to be u_*/f, found by nondimensionalizing eq. (4.11).

A consistent scaling of PBL velocity and stress by $\hat{u}_*$ and $\hat{\tau}_o$ $(= u_*\hat{u}_*)$, with z_o and u_*/f the respective length scales for the surface and outer layer, has become known as Rossby-similarity scaling after pioneering work of Rossby (1932) and Rossby and Montgomery (1935), although it was later investigators (see, e.g., Blackadar and Tennekes, 1968) who recognized the significance of using u_* rather than V_o for the outer layer velocity scale.

Rossby-similarity scaling provides a convenient rule of thumb for comparing oceanic and atmospheric scales. Assuming that the stress at the ice-air interface is comparable to the ice-water stress (which is likely if the ice is thin), then $(\rho u_*^2)_{atm} \simeq (\rho u_*^2)_{ocean}$; thus velocities and lengths in the OBL will be roughly 1/30 (square root of the density ratio) of those in the ABL. An interesting consequence of this is that a pressure ridge with, say, a 1 m sail compensated by a 5 m keel, has very different aspects when viewed from the different boundary layers. To the ABL, the feature is almost part of the surface roughness, being 2 to 3 orders of magnitude less than the ABL thickness. To the OBL, the ridge is a definite topographic feature, comparable to a 150 m high hill in the ABL. The ice undersurface is often pictured either as flat, or as a series of jagged ice blocks which provide nearly all the drag and stirring. Probably neither view is appropriate, and perhaps a better model would be to think of the under-ice OBL as comparable to atmospheric flow over rolling hills.

2.4 Boundary-Layer Transport

If the steady-state momentum equation (eq. 4.11) is integrated to the surface from some level below which no turbulent stress penetrates, a remarkable result ensues.

$$\text{if } \int_{-h}^{0} \hat{V}dz = \hat{\tau}_o \quad . \tag{4.12}$$

We define a transport vector, $\hat{M} = \int_{-h}^{0} \hat{V}dz$, which is the total volume transport per unit time in the boundary layer, and from eq. (4.12)

(4.13)

Without any consideration of how the turbulent mechanism works, eq. (4.13) implies that the steady-state volume flux in the OBL is oriented 90° clockwise (Northern Hemisphere) from the surface stress and equal in magnitude to τ_o/f. This effect, sometimes called geostrophic departure, was point out by Ekman (1905) and the concept is used extensively in calculating the effect of wind on deep ocean circulation (see, e.g., Stern, 1975).

2.5 Inertial Oscillations

The transport vector is also useful for demonstrating another flow phenomenon associated with the rotating reference frame: inertial oscillation. If eq. (4.6) is integrated in the same manner as eq. (4.12), we have

$$\frac{\partial \hat{M}}{\partial t} + if\hat{M} = \hat{\tau}_o \quad .$$

Now suppose a constant surface stress is applied at $t = 0$ to a system at rest. The solution to eq. (4.13) in this case is

$$\hat{M} = \hat{M}_s(1 - e^{-ift}) \tag{4.14}$$

where $\hat{M}_s = -i\hat{\tau}_o/f$ is the stationary solution. In the complex plane, the locus of solutions eq. (4.13) traces a circle in one inertial period, $1/2\pi f$ (~12.4 hr at 76°N), centered at $\hat{M}_s$. Note that the idealized inertial amplitude is equal to the steady-state transport. M is the average velocity of the OBL multiplied by its depth, so even the surface velocity may have a significant inertial component, with an associated drift trajectory that is cycloidal.

3. OBSERVATIONS

Over the past decade a number of experimental studies have helped focus our understanding of the upper ocean under pack ice. Two of special importance regarding turbulent transfer were the 1972 AIDJEX Pilot Study and the 1975–1976 AIDJEX Main Experiment.

The most complete measurements of mean flow and turbulence in the OBL were gathered during the 1972 Pilot Study by a group from the University of Washington under the direction of J. D. Smith. The measuring apparatus included small mechanical current meters mounted along three orthogonal axes, capable of measuring the mean flow and Reynolds stress tensor at eleven levels ranging from 2 to 54 m below the drifting ice. McPhee and Smith (1976) describe the experiment and results, many of which are used below to illustrate various PBL concepts. During the April wind storm from which the data were obtained, the ice drift was comparatively straight and

there was little indication of inertial oscillation in the ice/upper ocean system. On two different days of the same storm, abnormally steady conditions persisted: for about 5 hours in one case, and for 8 hours in a second. The data gathered constitute probably the most complete measurement ever made of mean and turbulent velocity structure in a fully developed, rotating boundary layer.

The AIDJEX Main Experiment, which maintained stations on the perennial pack over the Canada Basin for more than a year, lacked sophisticated equipment for precise current measurement in the OBL, but this was offset to some degree by the sheer volume of data collected. Two very important measurements were made at each of the manned stations without dropping an instrument in the water: highly accurate resolution of camp position normally at least once per hour, which provided surface velocity across the 100 km scale of the manned camp array, and continuous measurements of 10 m wind. During the summer when internal ice stress gradients were small, these data provided estimates of OBL surface velocity and stress that, as far as we know, are unparalleled in oceanographic studies. In addition, fixed current meters and daily STD and profiling current meter casts operated throughout the experiment.

3.1 Structure of the Steady OBL

Figure 3, drawn from data of McPhee and Smith (1976), shows mean flow measured at 9 levels through the mixed layer during the 1972 AIDJEX Pilot Study in both hodograph and profile form. Currents were averaged for 5 hours under very steady conditions. The pycnocline (steep density gradient) started at about 36 m below the ice. Actual currents were, of course, measured from the drifting ice, but are drawn relative to the measured current at 32 m, because concurrent measurements of the relative velocity of a fixed point on the sea floor showed that the actual current at the 32 m level was less than 2 cm s^{-1}, and was probably representative of $\hat{V}_g$.

Comparison of Figures 3 and 1 shows that, at least in its gross features, the observed flow is like the heuristic model outlined above. Near the ice, there is a region of high shear in the same direction as stress, but at greater depths the Coriolis effect is readily evident. The profiles provide an excellent example of geostrophic departure in that the integrated transport in the boundary layer is nearly all in the integral of the velocity component perpendicular to interfacial stress, despite a large surface component in the stress direction.

As detailed by McPhee and Smith (1976), turbulent stress was also measured during the 1972 experiment, and a reasonably exact

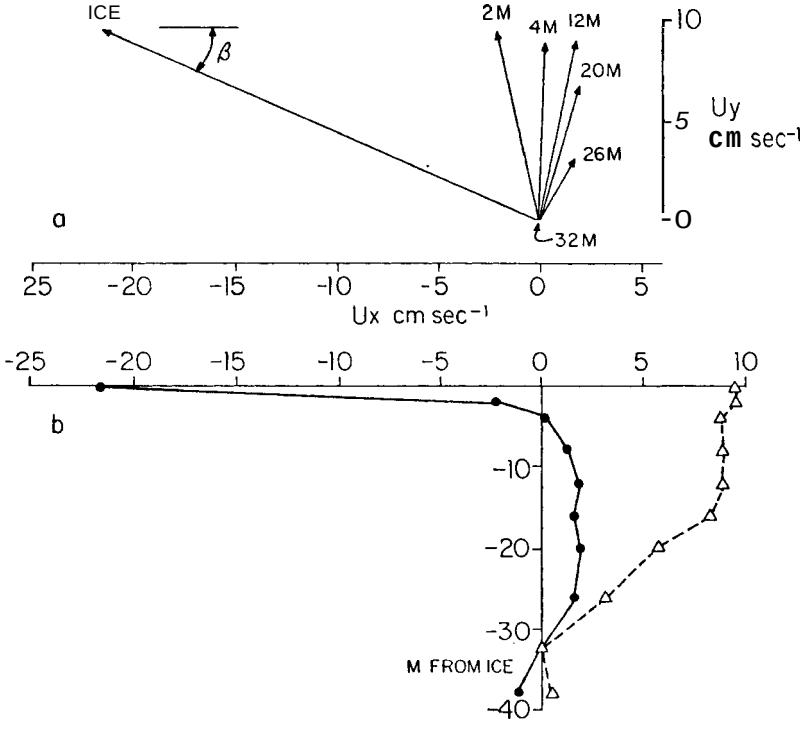

Fig. 3. Currents averaged for 5 hours, measured at AIDJEX Pilot Study station Jumpsuit, 12 April 1972. Data are referenced to the 32 m level, taken to be the geostrophic current due to sea surface ships.

estimate of interfacial stress was obtained. During the time of measurements shown in Figure 3, it was about 1 $cm^2\ s^{-2}$. At latitude 76°, f = 1.4 x $10^{-4}\ s^{-1}$, therefore the PBL scale depth, u_*/f, was about 70 m. Figures 4 and 5 show the six independent components of the Reynolds stress tensor measured at 9 levels, compared with results from numerical models of turbulent structure for the steady horizontally homogeneous ABL. Note that the comparison with atmospheric models is made using the Rossby-similarity nondimensionalization -- the correspondence between the ABL models and the oceanic data lends credence to that approach.

In the 1972 data, it was clear that the simple momentum equation, eq. (4.11), was not satisfied, and that some other factor was affecting the mean force balance. The explanation for this other force probably lies in the fact that the ice undersurface was not homogeneous, and horizontal variations in the topography of the ice underside would cause local accelerations. It was possible to argue consistently that such a "form drag" force could account, at least in part, for differences in both the mean flow profile and the turbulent stress components from what would be expected in a horizontally homogeneous flow (ibid.). This is an important point

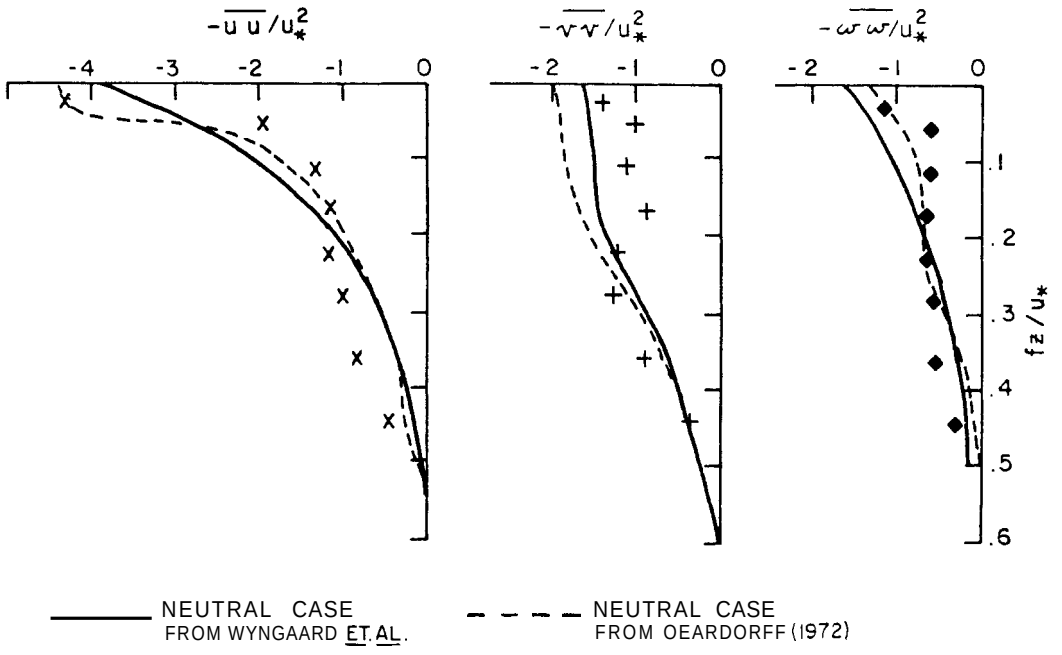

Fig. 4. Diagonal elements of the nondimensional Reynolds stress tensor corresponding to the mean currents shown in Figure 3.

regarding surface velocity. Since the ice often presents a more or less rigid surface over distances a couple of orders of magnitude greater than the OBL depth, it acts to integrate the drag contributions from many different ice types. Thus, the surface velocity that would correspond to the local turbulence structure and surface roughness if the surface were uniform, is not necessarily the one measured. From the 1972 data, we estimated that the "skin friction" drag measured under relatively smooth, undeformed ice was about half of the total drag contribution. Presumably the remainder was made up of contributions from rougher ice, and from form drag across pressure ridge keels.

Because of the form drag effect, there was no clear-cut relation between the mean velocity shear and the Reynolds stress in the 1972 measurements. Despite this, peaks in the spectra of vertical velocity fluctuations indicated length scales for the most energetic eddies, from which an effective eddy viscosity could be calculated. Results of those calculations are shown in Figure 6, again compared to ABL models. Note that past a distance of about 0.1 u_*/f from the interface, the eddy viscosity no longer increases. This is evidence that there is some limiting size to

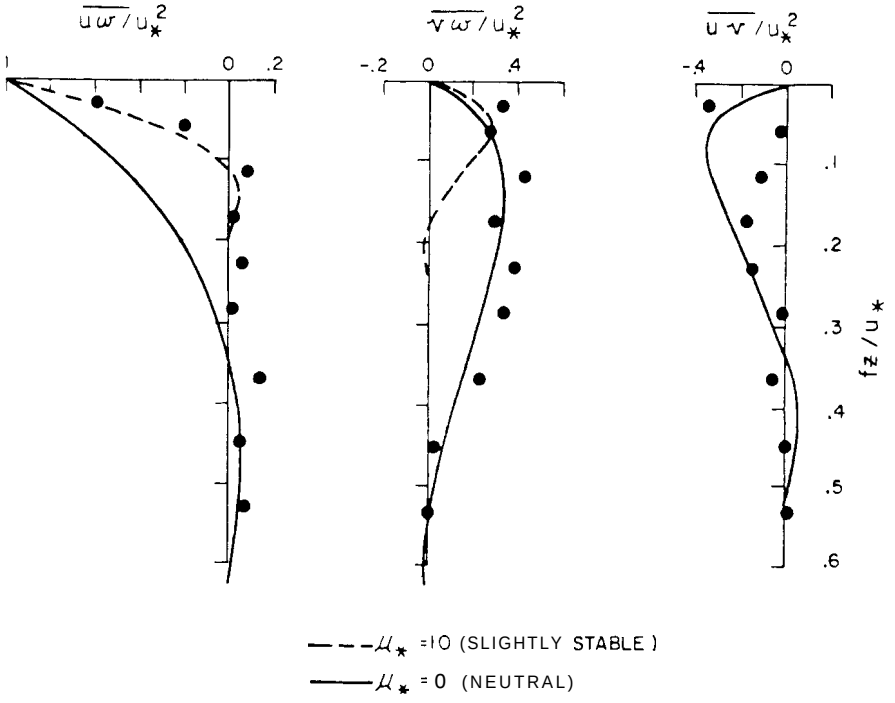

Fig. 5. Same as Figure 4, except shear stress elements. Curves are from Businger and Arya (1974).

the turbulent eddies that is considerably smaller than the scale of the boundary layer itself.

3.2 Mean Drift Statistics

One of the most basic but elusive measurements for testing steady-state PBL theory is simultaneous monitoring of surface stress and free-stream velocity. For the ABL, local surface-layer measurements of stress must be related to the mean drag over an area of at least several kilometers squared (which is straightforward only if the surface is exceptionally uniform), and this in turn must be related to the geostrophic wind, including any thermal wind effects due to horizontal temperature gradients. Adding to the difficulty in most temperate-zone experiments are time-dependent changes as the ABL goes through the diurnal cycle of heating and cooling.

In the open ocean the situation is worse. Even given that surface air stress can be measured precisely (no simple matter), determining surface or near surface currents accurately is a real challenge, particularly with well developed waves. A proper oceanic theory for near surface currents should consider gravity wave

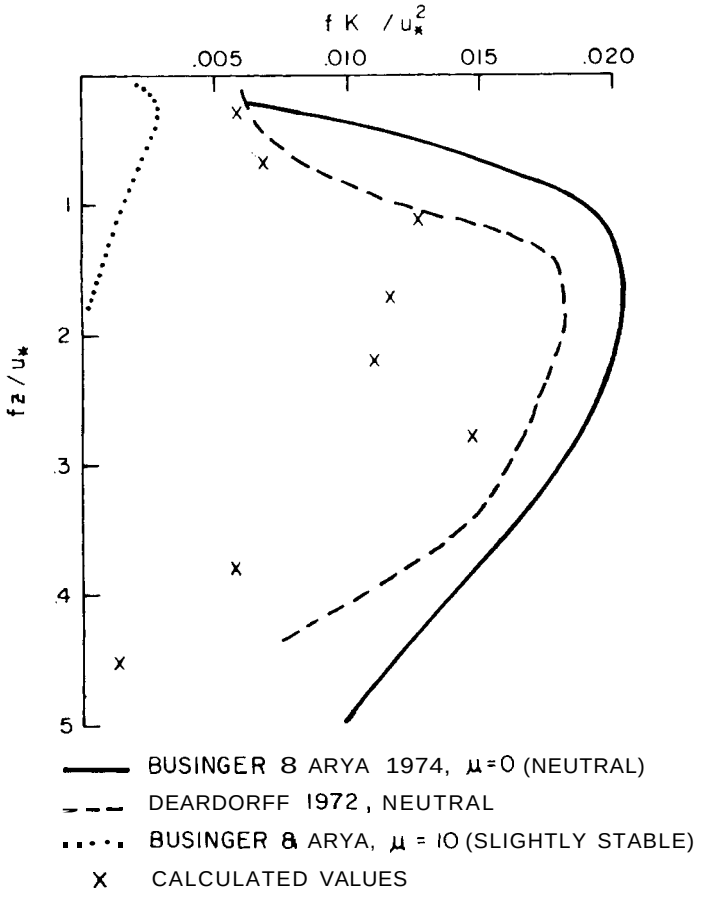

Fig. 6. Nondimensional eddy viscosity calculated from peaks in spectra of vertical velocity compared with ABL models (from McPhee and Smith, 1976).

effects like Stokes drift, and comparison with data must include an estimate of oceanic geostrophic flow.

Viewed in this light, an ice drift experiment offers exciting possibilities, provided one can identify periods of "free drift", when the internal stress gradient in the ice is negligible in the momentum balance as sketched in Figure 1. Under such conditions, the air stress can be estimated closely from surface wind measurements; surface velocity can be ascertained accurately from satellite navigation; reasonable estimates for the mean ice mass and undisturbed geostrophic flow can be made; and from these data, $\hat{V}_o$ and $\hat{\tau}_o$ calculated. In the central Arctic, dynamic height contours (e.g., Newton, 1973) are used to calculate surface geostrophic flow, which is found to be small compared with the usual ice drift. Because of the relative uniformity of the upper ice surface when

compared with the ABL depth scale (~1 km), an estimate of air stress at one location is representative of a large area, provided allowance for pressure ridge sails is made. (The same cannot be said of point measurements in the ocean, because of the disparity in scales.) Therefore, the major problem is identifying free drift periods.

Although somewhat paradoxical, the best time for testing the steady-state relationship between surface velocity and stress during the AIDJEX Main Experiment occurred during the melt season of 1975 when inertial oscillation of the ice cover was most pronounced. The presence of inertial motions indicates that internal ice forces are small, and there is evidence that the mean drift of the ice is not much affected by the oscillations (McPhee, 1980b). Analysis and results of a study of drift, wind, and currents over the 60 day melt season are described by McPhee (1979). The aim of that work was to determine statistically the form of the stress to surface velocity relationship and to examine it in terms of PBL theory. Figure 7 shows the main result, which is a scatter diagram of τ_o calculated from the momentum balance of Figure la plotted against relative ice speed. The solid line is a best fit exponential of the form $\tau_o = aV^b$, where a and b are determined from logarithmic regression of smoothed data taken from all camps over the 60 day period. The exponent, b, was found to be 1.78 $\pm$ 0.12 at the 90% confidence level. Over a whole range of plausible values for ice mass and 10 m wind drag coefficient, this result varied by only a few percent. The relationship is obviously not linear (b = 1), but also shows a slight but significant difference from quadratic (b = 2). The dashed curve is described in the next section, where the shape of the curve is shown to support the Rossby-similarity hypothesis.

3.3 Inertial Oscillations

Most measurements of mixed layer currents in the open ocean show a strong periodic signal at the inertial frequency. Hunkins (1967) observed that summer speed records from deep current meters suspended near Fletcher's Ice Island (T-3) also contained an inertial signal, which he interpreted as evidence that T-3 and the surrounding ice pack were drifting with cycloidal loops at the inertial period. In the early AIDJEX pilot experiments, the inertial component in ice drift was detectable but of small amplitude. During the 1975 melt season of the AIDJEX Main Experiment, however, there were large inertial waves in both relative velocity records from current meters suspended below the mixed layer and in the surface drift velocity. Figure 8 shows an example of the latter from a 12-day period during August, 1975. The oscillations were initiated by the passage of two atmospheric fronts, and are described in detail by McPhee (1980a).

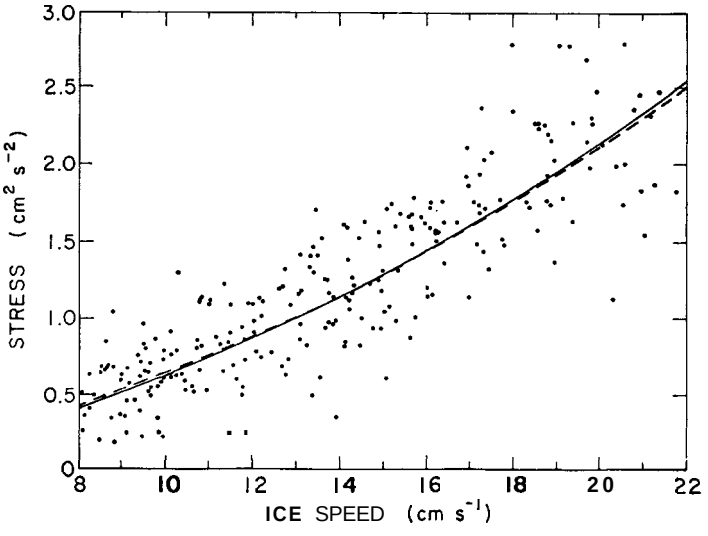

Fig. 7. Kinematic interfacial stress versus relative ice speed from smoothed AIDJEX data, summer 1975. Solid line is best fit exponential, $\tau_o = 0.0104V^{1.78}$; dashed line is theoretical result described in text (from McPhee, 1979).

In analyzing inertial oscillations, a shorthand introduced by H. Perkins (1970), which he terms complex demodulation, is helpful. A complex inertial wave, $\hat{A}e^{-ift}$, is fit in a least-squares sense to the velocity record over a specified period, usually about twice the inertial period. The complex coefficient, $\hat{A}$, (which may be called a phasor) describes the phase and amplitude of the inertial wave. A time series of phasors may be analyzed to determine amplitude decay and phase shift of a particular wave train. Figure 9 shows such a study for surface velocity, one component of which is shown in Figure 8. The three manned stations analyzed spanned about 190 km west to east in a fairly narrow latitude band. There is a remarkable similarity in their response to the first frontal system. This is shown more clearly in Figure 10, obtained by adjusting the phase at the west and central stations by constant amounts, calculated assuming the fronts to propagate eastward at 60 km hr^{-1}. The striking uniformity in response to the first storm probably means that an oceanic coupling accompanies rapidly moving atmospheric systems. The second storm was slower moving, and the inertial response does not show the same horizontal coherence.

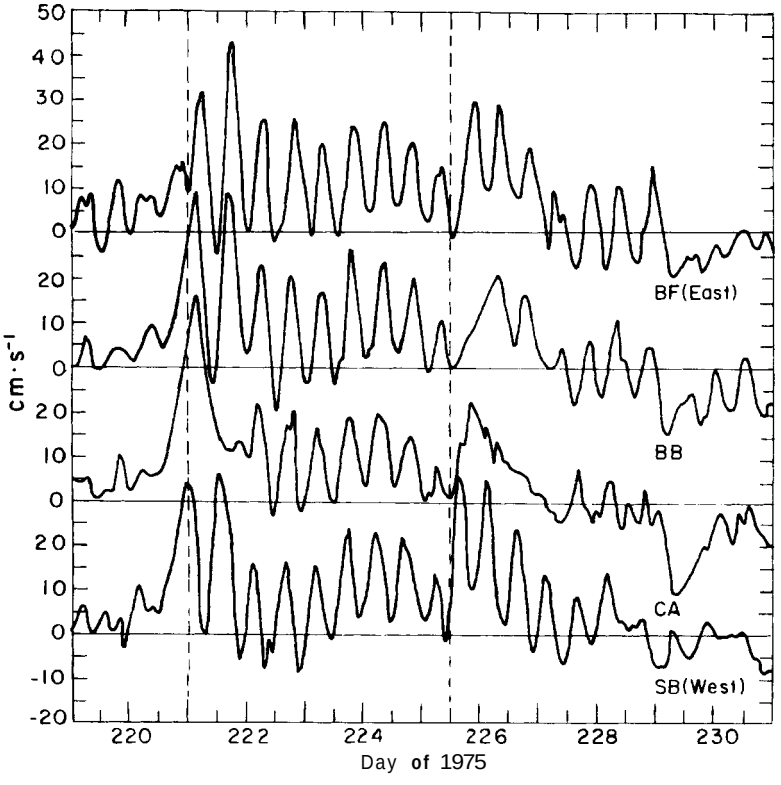

Fig. 8. Zonal (eastward) component of surface velocity determined from satellite positioning at four AIDJEX stations, showing strong inertial period motion.

4. THEORIES

4.1 OBL Momentum Transfer

Aside from intrinsic interest, there are two rather different motives for studying turbulent transfer in the upper ocean. In the first case, one is interested in how turbulence influences mean currents: a prime example is predicting surface (ice) velocity given the interfacial stress field. In the second, interest is directed more toward scalar properties of the mixed layer: e.g., predicting changes in mixed-layer temperature and salinity as a function of surface fluxes. In principle, the distinction is artificial, but in practice sometimes useful. For example, the impact on surface velocity of turbulent salinity flux at the base of the mixed layer appears to be small and often negligible unless the mixed layer is abnormally shallow (McPhee, 1979); on the other hand, it is crucial for understanding how mixed layer salinity and temperature respond to surface mixing. Viewing the same problem from these different perspectives has led to quite different theoretical formulations: e.g., second-order turbulent closure as

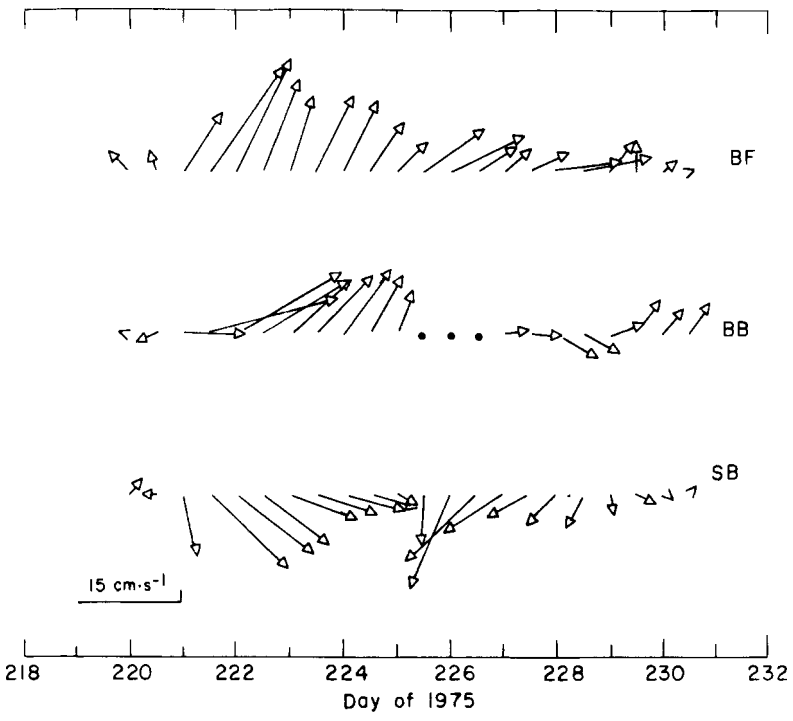

Fig. 9. Phasors describing the inertial art (amplitude and phase) of surface velocity at three AIDJEX camps (from McPhee, 1980a).

opposed to "slab" mixed-layer models. [The interested reader may wish to compare the approach of Mellor and Durbin (1975) with that of Niiler (1975).]

This section addresses primarily the question of momentum flux, particularly the relationship between surface stress and velocity. We shall review briefly the theoretical background of PBL momentum flux and outline a simple turbulence model that explains many observed features. The framework includes modifications to turbulent drag caused by rapid surface melting. In a later section on the evolution of the summer pycnocline, the model will be extended to include buoyancy flux in density gradients at lower levels.

4.2 "Geostrophic" Drag

Experience with laboratory studies of pipe and flat plate flow has shown that if the flow is laminar (exchange dominated by molecular processes), the drag relationship is linear, $\tau_o \propto V_o$; whereas in turbulent flow the drag is more nearly quadratic, $\tau_o \propto V_o^2$.

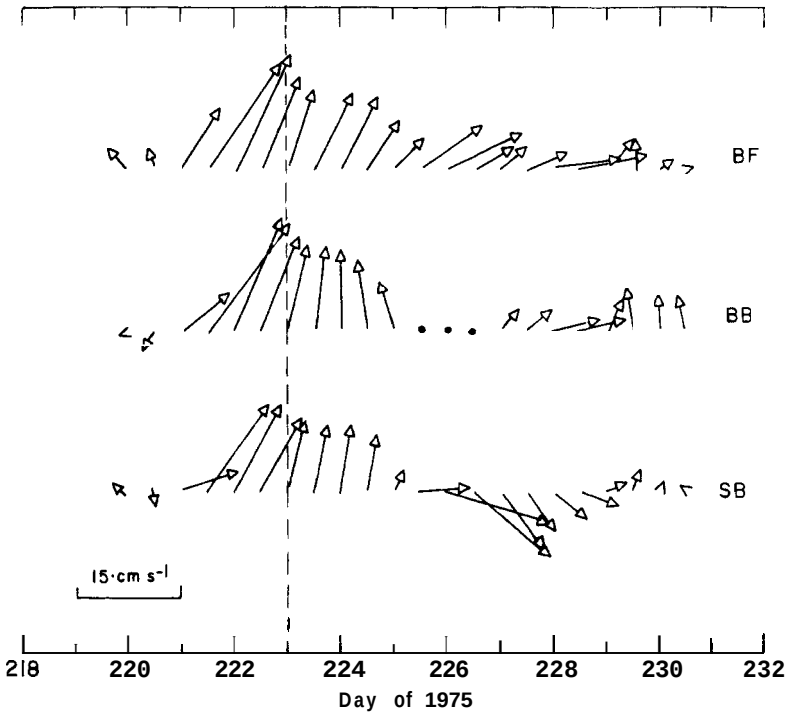

Fig. 10. Same as Figure 9, except phase adjusted by arrival time difference assuming that the generating disturbance moved eastward at 60 km hr^{-1}. Note the remarkable uniformity during the first half of the record despite zonal span of 190 km.

With quadratic drag, $V_o \propto u_*$, and it is convenient to consider the nondimensional surface velocity, $\hat{v}_o = V_o/\hat{u}_*$. $\hat{v}_o$ is complex: its real part lies in the direction of surface* stress; its imaginary part 90° counterclockwise. In polar form $v_o = v_o e^{-i\alpha}$ where a is the boundary layer turning angle. The magnitude v_o is the inverse of what is called geostrophic drag for the atmosphere, i.e.,

$$u_* = (1/v_o)V_o, \qquad \tau_o = \left(\frac{1}{v_o}\right)^2 V_o^2$$

Note that if drag is quadratic, the magnitude of the nondimensional surface velocity is constant.

4.3 Ekman Theory

Ekman's original formulation of the PBL problem (Ekman, 1905) has served as a paradigm for most subsequent PBL theory. Among

other things, Ekman showed that for an eddy viscosity, K, independent of depth, the steady momentum equation (eq. 4.11) is

$$\frac{\partial^2 \hat{V}}{\partial z^2} = \frac{if}{K}\hat{V} \tag{4.15}$$

with solution

$$\hat{V}(z) = \hat{V}_o e^{\hat{\delta} z} \quad , \qquad \hat{\delta} = (if/K)^{1/2} \quad .$$

$\hat{\delta}z$ is complex so the factor $e^{\hat{\delta}z}$ both attenuates and rotates the velocity with increasing depth. From $\hat{\tau} = K\frac{\partial \hat{V}}{\partial z}$, the nondimensional surface velocity is

$$\hat{v}_o = \frac{\hat{V}_o}{\hat{u}_*} = \frac{u_*}{(fK)^{1/2}} e^{-i\pi/4} \tag{4.16}$$

whence the well known result that the surface velocity is 45° cum sole, when the eddy viscosity has no depth dependence.

The Ekman solution (eq. 4.16) is often taken to be synonymous with linear, or Newtonian, drag because u_* appears on the right-hand side. However, Ekman realized that K would vary depending on surface stress conditions, and in fact, he derived an empirical expression relating the Ekman depth, $D = \pi(2K/f)^{1/2}$, to the surface wind speed, u_s, and latitude, λ:

$$D \propto u_s/(\sin \lambda)^{1/2} \quad . \tag{4.17}$$

The friction velocity is proportional to the near surface wind, so Ekman's expression results in $K = K_E u_*^2$ (where K_E is constant), which makes eq. (4.16) a quadratic drag law consistent with other turbulent flows.

It is interesting that Ekman came so close to outlining what has become known as Rossby similarity. Had he chosen instead of eq. (4.17) the closely related expression

$$D \propto u_s/\sin \lambda \propto u_*/f \quad ,$$

his theory would have provided an eddy viscosity

$$K = K_* u_*^2/f \quad , \tag{4.18}$$

which implies a scaling velocity, u_*, and mixing length, $K_* u_*/f$ in the basic mixing length formulation.

For future reference, consider the Ekman problem using eq. (4.18) for eddy viscosity with nondimensional length, stress, and velocity: $\hat{\xi}$, $\hat{T}$, and $\hat{v}$ defined by $z = u_* \hat{\xi}/f$, $\hat{\tau} = \hat{T} u_* \hat{u}_*$, and $\hat{V} = \hat{v} \hat{u}_*$. Rather than solving directly for $\hat{v}$, we write the nondimensional form of eq. (4.11):

$$i\hat{v} = \partial \hat{T}/\partial \hat{\xi} \quad , \tag{4.19}$$

differentiate and substitute $\partial \hat{v}/\partial \hat{\xi} = \hat{T}/K_*$ to obtain

$$i\hat{T}/K_* = \partial^2 \hat{T}/\partial \hat{\xi}^2 \quad . \tag{4.20}$$

With $\hat{\gamma} = (i/K_*)^{1/2}$ and boundary conditions $\hat{T}(-\infty) = 0$, $\hat{T}(0) = 1$, and $\hat{v}(-\infty) = 0$, solutions are

$$\hat{T}(\xi) = e^{\hat{\gamma}\xi} \tag{4.21}$$

$$\hat{v}(\xi) = (iK_*)^{-1/2} e^{\hat{\gamma}\xi} = K_*^{-1/2} \hat{T} e^{-i\pi/4} \quad . \tag{4.22}$$

Hodographs of the solutions are shown in Figure 11 for $K_* = 0.021$.

While the difference may at first seem trivial, there is a subtle but important shift in perspective when the stress equation (eq. 4.20) is solved rather than the momentum equation. The heuristic view of the PBL developed in Section 2.1 requires rapid velocity change in the direction of surface stress (real axis) across the surface layer, but little change in the transverse (imaginary) component, so that the drift angle is about half of 45°. The Ekman solution for velocity in the surface layer does not predict this behavior. On the other hand, stress is presumed to change little across the surface layer, and since the change in $\mathrm{Im}(\hat{v}_o)$ is small, we can approximate the real component of nondimensional stress from eq. (4.19) by

$$\mathrm{Re}(\hat{T}) = 1 + \mathrm{Im}(\hat{v}_o)\, \xi \quad .$$

A Taylor series expansion for the stress solution eq. (4.21) is

$$\mathrm{Re}(\hat{T}) = 1 + \mathrm{Re}(\hat{\gamma}\xi) = 1 - (2K_*)^{1/2} \xi \quad .$$

But from eq. (4.22), this is also $1 + \mathrm{Im}(\hat{v}_o)\xi$. Thus, while the real component of surface layer velocity is not well described by depth independent eddy viscosity, there are indications that stress is. This idea can be explored further with the help of numerical models.

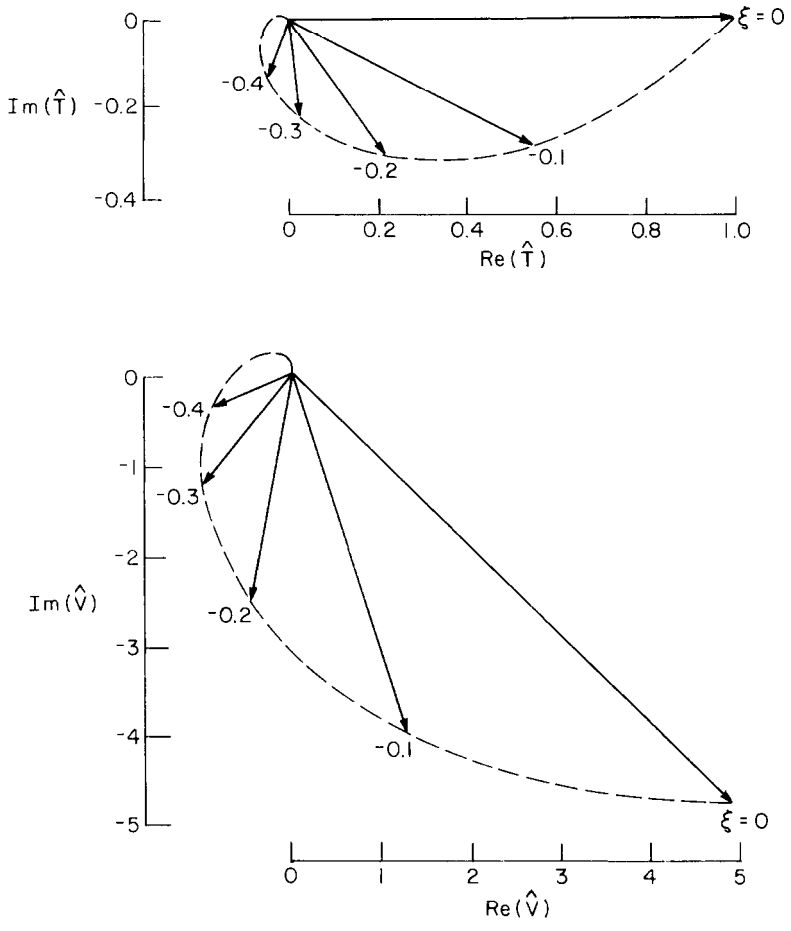

Fig. 11. The Ekman solution for nondimensional turbulent stress and mean velocity. Numbers beside hodographs indicate nondimensional depth.

4.4 Numerical PBL Models

Numerical methods for solving the boundary layer equations have elucidated much about the structure of PBL turbulence. The models range in complexity from "brute force" three-dimensional integration of the complete equations over a relatively fine mesh, where the only parameterization comes at the sub-grid scale (Deardorff, 1972), to solving the mean momentum equation given an analytic expression for the eddy viscosity. An intermediate class, referred to as "second-order-closure" models, solves simultaneous equations for mean and first-moment variables, the latter equations using some parameterization for terms involving second and higher

moments. A summary of turbulent closure schemes, with hierarchical ranking, is given by Mellor and Yamada (1974). Figures 4, 5 and 6 compare data from the underice OBL with models of Deardorff (1972, average of ten realizations of time-dependent, three-dimensional numerical integration); Wyngaard et al. (1974, second-closure, simultaneous solution of 13 partial differential equations); and Businger and Arya (1974, steady state, mean momentum equation with prescribed analytic K_m distribution).

The Businger and Arya (1974) model, which for the neutrally buoyant PBL produces profiles of mean velocity and turbulent stress similar to the steady-state solutions of Wyngaard et al. (1974), is an instructive extension of the nondimensional Ekman theory of the previous section. Starting from the nondimensional stress equation (eq. 4.20), an expression for K_m is prescribed (the example here is for the neutral case only, although their treatment includes stable surface buoyancy)

$$K_* = k\xi e^{-|v_s|\,\xi} \quad . \tag{4.23}$$

K_* is an exponentially attenuated, linear function of ξ, which goes to $K_* = k\xi$ for ξ small; and v_s is the transverse (imaginary) component of surface velocity. Using an initial estimate for v_s, eq. (4.20) is solved; the calculated value of v_s is used to obtain a new solution; and the procedure is repeated as long as the change in v_s exceeds a given tolerance. Figure 12 from McPhee (1979) shows results of this model adapted to the OBL. The surface velocity is found by integrating the stress, solved by setting $\hat{T} = 1$ at $\xi = \xi_o$, where $\xi_o = fz_o/u_*$. The inverse of ξ_o is called the "surface-friction Rossby number" and is the ratio of the outer layer scale, u_*/f, to the surface layer scale, z_o. The dashed curve in Figure 7 (ibid.), which shows τ_o vs. V_o, is the locus of solutions for V_o given u, in the range shown, with $z_o = 10$ cm. In terms of least-squares logarithmic regression of $\tau_o = aV_o^b$, the exponent, b is 1.70 ± 0.00 for the solution points. To within experimental uncertainty, this is direct confirmation that Rossby-similarity scaling governs the underice ORL.

4.5 Two Layer Theories

Before the PBL equations could be routinely solved with computers, the outer and surface layers were often reconciled by noting that since stress was nearly constant through the logarithmic surface layer, an analytic, Ekman-like solution for the outer layer, which used surface stress as it boundary condition, could be matched to a unidirectional surface layer profile (e.g., see Rossby and Montgomery, 1935). This basic approach has been used extensively to calculate oceanic drag on sea ice, under a number of different assumptions about the two layers. Several such

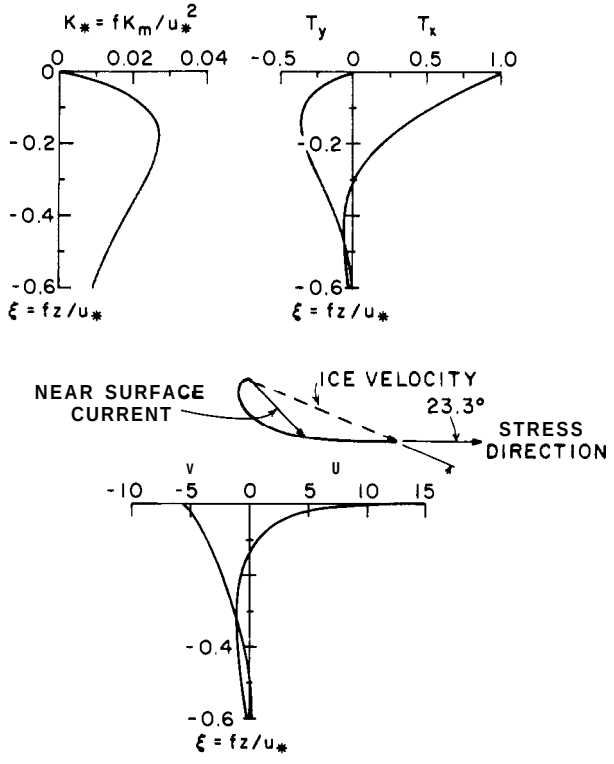

Fig. 12. Adaptation of Businger and Arya (1974) model to the neutral OBL. K_* is an exponentially attenuated, linear function of $\xi = fz/u_*$.

models (among others, Shuleikin, 1938; Reed and Campbell, 1962; Rothrock, 1975) are discussed by McPhee (1982) and compared with the AIDJEX drag relationship shown in Figure 7. A conclusion of that work was that only those simple models that somehow incorporated Rossby-similarity scaling for the outer and surface layers agreed with the shape of the stress-surface speed curve.

The simplest two-layer approach with u_* and f scaling is diagrammed in Figure 13 from McPhee (1982). We assume, first, that nondimensional eddy viscosity increases linearly with depth until it reaches the value, $K_* = k\xi_N$ (where ξ_N is the nondimensional thickness of the surface layer), which it takes for all greater depths; and second, that stress is constant ($\hat{T} = 1$) in the layer where K_* varies. The total nondimensional surface velocity is then, the sum of the Ekman surface velocity and the logarithmic velocity through the surface layer, i.e. :

$$\hat{v}_o = \hat{v}_{oE} + \frac{1}{k}\ln(\xi_N/\xi_o) = (k\xi_N)^{-1/2}\, e^{-i\pi/4} + \frac{1}{k}\ln(Ro_*\xi_N) \qquad (24)$$

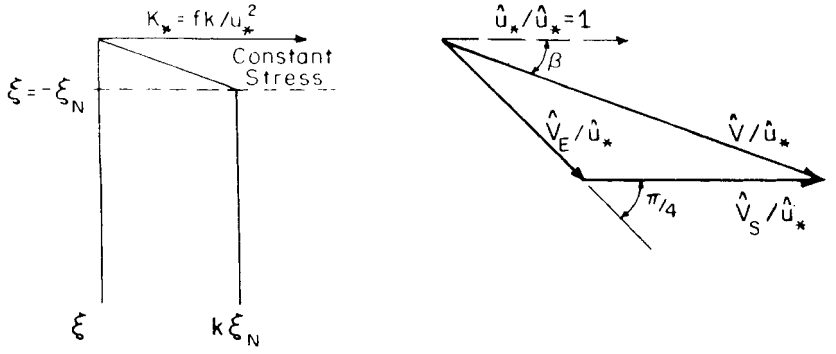

Fig. 13. Simple two-layer approach in which stress is constant and K_* varies linearly through a surface layer of thickness ξ_N. The surface velocity is vector sum of Ekman velocity, $\hat{V}_E$, and logarithmic shear across the surface layer, V_S.

where ξ_o is again the inverse of the surface-friction Rossby number, $R_{o_*} = u_*/fz_o$. With a proper empirical choice of ξ_N and z_o (for the AIDJEX data, $\xi_N = 0.045$, $z_o = 23$ cm), the shape of the τ_o vs. V_o curve and the boundary layer turning angle implied by eq. (4.24) are almost identical to the results of the Businger and Arya model. Therefore eq. (4.24) can be considered an acceptable drag law for sea ice, although conceptually it has some unsatisfying features which we shall address below.

Equation (4.24) provides a simple explanation of why the drag law is somewhat less than quadratic, despite the fact that the turbulence is fully developed. Recall that quadratic drag requires the nondimensional surface velocity to be constant. For a given surface roughness, all the terms on the right-hand side of eq. (4.24) are constant except $(\ln u_*)/k$, which contributes to the real component. As u_* increases, the nondimensional real component also increases; v_o increases slightly and the turning angle decreases. Therefore, to double the surface speed requires a little less than doubling u_*, and the drag is less than quadratic. This is the essence of Rossby-similarity theory for geostrophic drag, although it is often presented in a different way (e.g., Blackadar and Tennekes, 1968).

4.6 Surface Buoyancy

To this point we have tacitly assumed the OBL to be neutrally buoyant, meaning that surface freezing or melting has no effect on the turbulence. It is well known, however, that buoyancy (i.e., the gravitational acceleration encountered by turbulent eddies when the fluid is not of uniform density) plays an important role

in ARL dynamics, and we might anticipate the same for the underice ORL, especially with extreme melting or freezing.

Again there are two rather distinct viewpoints in considering surface buoyancy effects. On the one hand, while introduction of fresh meltwater throughout the summer is bound to have a major impact on OBL salinity, its effect on turbulent drag may be unimportant. On the other hand, if melting rates are extreme, as they might be near the ice-margin front, the drag could be reduced considerably. In this section the emphasis is on how surface buoyancy affects surface drag.

So far we have considered two mixing length scales for turbulence in the OBL: kz in the surface layer, and a maximum mixing length which is some small fraction of u_*/f in the outer layer. When density variations enter the problem in the form of salinity changes at the interface with the ice, a third length scale, the Obukhov length, L, may be used to quantify how the turbulent flux of density variations, $\overline{\rho' w'}$, modifies the momentum exchange.

The surface layer turbulent kinetic energy (TKE) equation consists of a balance between shear production and buoyant production on one side against flux divergence-pressure transport and viscous dissipation on the other. (Tennekes and Lumley, 1972, Chapter 3, present a clear derivation and discussion of the TKE budget.) If the TKE equation is nondimensionalized by u_*/kz, the shear production term is

$$\phi_m = \frac{kz}{u_*} \left(- \frac{\overline{\hat{v}' w'}}{u_*^2} \right) \frac{\partial \hat{V}}{\partial z} \tag{4.25}$$

and the buoyant production term is z/L where

$$L = \rho_o u_*^3 / (gk\overline{\rho' w'}) \tag{4.26}$$

The TKE equation may be written

$$\phi_m - z/L = \phi_D + \phi_E \tag{4.27}$$

where ϕ_D represents the nondimensional pressure-transport-flux divergence and ϕ_E is the nondimensional viscous dissipation.

The nondimensional TKE (actually, rate of energy transfer) eq. (4.27) provides a physical interpretation of L. In the surface layer the shear production, ϕ_m is of order one (see eq. (4.9) and in the absence of buoyancy, the size of the energy-containing eddies is of order z. If L is positive (stable) and also of order z,

then the buoyancy term is comparable to ϕ_m, but of opposite sign, so that the total TKE production rate is much reduced. For $|L|$ large compared to z, the buoyancy term is small and shear production dominates. For L small and positive, turbulence is quelled by the gravitational force; for L small and negative (unstable), the turbulence derives most of its energy from 'buoyant acceleration rather than shear.

In the simplified view of the OBL developed above, we inferred from data that the maximum mixing length ($\ell_m = u_* k\xi_N/f$) is some small fraction of u_*/f. It seem reasonable that if L is several times as large as ℓ_m, turbulence through the entire boundary layer will not be much affected by buoyancy. This provides a way of estimating how important surface freezing and melting may be: If $f|L|/u_* >> k\xi_N$ (about 0.02), we are safe in treating the OBL as neutral. L is related to ice growth rate, d, as follows. From eq. (4)

$$\frac{\overline{\rho'w'}}{\rho_o} \simeq -\alpha_\theta \overline{w'\theta'} + \alpha_s \overline{w'S'} \ .$$

Sea ice is typically only 15–20% as saline as the water from which it grows, so that when freezing (melting) occurs, there is a flux of saltier (fresher) water across the interface. The surface salinity flux is given by

$$\overline{w'S'}\Big|_o = -\frac{\rho_{ice}}{\rho_o}\left(\frac{S_w - S_{ice}}{1000}\right) d = -\Delta_s d$$

where $S_w - S_{ice}$ is the salinity difference expressed in per mille.

Unlike fresh water, the coefficient of thermal expansion for seawater, α_o, increases monotonically from the freezing point. Since α_o is small for temperatures near freezing, thermal expansion has little effect on density and can often be neglected (see, e.g., Neumann and Pierson, 1966), in which case

$$\overline{\rho'w'}\Big|_o \simeq \alpha_s \overline{w'S'}\Big|_o = -\alpha_s \Delta_s d \ .$$

The nondimensional Obukhov length is then

$$L_* = -fu_*^2/(gk\alpha_s\Delta_s d); \qquad [\theta < 0^oC] \ .$$

From changes in upper ocean salinity observed during the AIDJEX melt season, the maximum melting rate was estimated to be about 2.4 cm d^{-1}, or 2.8 x 10^{-5} cm s^{-1}. Under typical drift conditions,

u, was about 1 cm s^{-1}, and with Δ_S = 0.0225, α_S = 0.8, f = 1.4 x 10^{-4} s^{-1}; from (28), L, = 0.71. This is considerably larger than $k\xi_N$, thus for practical purposes we may normally neglect changes in drag due to melting, at least well within the limits of the perennial pack. In a pack with much multiyear ice, it is hard to imagine spatially average freezing rates of much more than a few cm per day, so the same arguments should apply for unstable conditions.

Near the ice margins, or in an unconsolidated pack, the situation may be quite different. In winter, cold winds blowing off the pack can expose large expanses of open water to rapid freezing, creating a widespread region of unstable boundary flux in the ocean as well as the atmosphere. Often a sharp front in mixed-layer temperature exists near the ice margin; if floes are blown into the warmer water, they will melt much more rapidly than the pack of the central Arctic, and may have a quite significant effect on oceanic drag (McPhee, 1982).

4.7 A Two-Layer System Stabilized by Surface Buoyancy

In a recent paper (McPhee, 1981) we developed analytic expressions, based on the mixing length arguments set forth above, for stress and mean velocity in the steady PBL stabilized by surface buoyancy. The theory, which borrows from scaling concepts developed by Zilitinkevich (1975) and from heuristic arguments of Businger and Arya (1974), is here briefly outlined; more complete details may be found in the paper.

From the two-layer premise, we make the following assumptions:

1. Scales formed from the parameters u_*, f, and L exist that, when used to nondimensionalize the mean velocity and turbulent stress structure in the outer layer of any flow, result in "universal" profiles of those quantities. This implies immediately that there is only one nondimensional eddy viscosity governing turbulence in the outer layer, at least for the rather restricted class of boundary layers being considered (i.e., steady-state, stabilizing buoyancy flux).

2. Turbulent stress is not affected by changes of eddy viscosity in the surface layer. This is not really a very severe restriction: In most surface layer studies stress is assumed constant through the surface layer -- here we require only that its variation across the layer is not sensitive to the magnitude of the eddy viscosity, which is given the universal value of the outer layer.

3. Finally, we assume that the maximum mixing length varies between two limits: In the neutral case it is $\ell_m = k\xi_N u_*/f$ as

before; and under highly stable conditions it is proportional to L. The proportionality constant is the critical flux Richardson number, R_c, following the reasoning of Zilitinkevich (1975). The simplest expression including these two limits is

$$\ell_m = \frac{u_* \xi_N}{f} \left(1 + \frac{\xi_N}{R_c} \cdot \frac{u_*}{fL}\right)^{-1} \tag{4.29}$$

Let $\mu_* = u_*/fL$ (the ratio of the neutral PRL scale to the Obukhov length). Substitution of eq. (4.29) into the expression for K_* (which is also equal to $k\xi_N$) yields the following nondimensional parameters:

$$\text{Depth: } \xi = fz/u_*\eta_* \qquad \text{Velocity: } \hat{u} = \eta_*\hat{V}/\hat{u}_*$$

$$\text{Stress: } \hat{T} = \hat{\tau}/u_*\hat{u}_* \qquad \text{Eddy viscosity: } K_* = fK/u_*^2\eta_*^2 \tag{4.30}$$

where $\eta_* = (1 + \xi_N\mu_*/R_c)^{-1/2}$. η_* is a stability parameter less than or equal to one (the neutral limit is one).

The velocity structure within the surface layer is governed by a nondimensional eddy viscosity which derives from the log-linear profile observed in the atmosphere:

$$K_* = -\frac{k\zeta}{\eta_*}(1 - \beta\mu_*\eta_*\zeta)^{-1}$$

where

$$\beta = \left(\frac{1}{R_c} + \frac{1}{\mu_*\xi_N}\right)(1 - \eta_*) \quad .$$

In the surface layer ($|\zeta| < \xi_N$) velocity is obtained by integration of stress divided by K_*, resulting in the following equations for stress and velocity in the entire PBL.

$$\hat{T} = e^{\hat{\delta}\zeta}$$

$$\hat{u} = \begin{cases} -i\hat{\delta}e^{\hat{\delta}\zeta} & ;\zeta \le -\xi_N \\ -i\hat{\delta}e^{-\hat{\delta}\xi_N} - \frac{\eta_*}{k}\left[\ln\frac{|\zeta|}{\xi_N} + (\hat{\delta} - a)(\zeta + \xi_N) - \frac{a}{2}\hat{\delta}(\zeta^2 - \xi_N^2\right]; \\ \qquad\qquad \zeta_o \ge \zeta > -\xi_N \end{cases}$$

where $a = \eta_*(1/\xi_N + u_*/fLR_c)(1 - \eta_*)$. The "geostrophic drag law" (i.e., the nondimensional surface velocity) is

$$\hat{u}_o = \eta_* \frac{\hat{V}_o}{\hat{u}_*} = -i\hat{\delta} e^{-\hat{\delta}\xi_N} - \frac{\eta_*}{k}\left[\ln \frac{|\zeta_o|}{\xi_N} + (\hat{\delta} - a)\xi_N + \frac{a}{2}\hat{\delta}\xi_N^2\right]. \tag{4.29}$$

The average ice drift and stress during the summer part of the AIDJEX Main Experiment were used to determine the one free constant in the theory, $\xi_N = 0.052$. Figure 14 shows the similarity model for stress and velocity in the outer layer compared with the neutral ($\mu_* = 0$) results of Businger and Arya (1974). Note the close correspondence in stress, even with constant K_*. Note also that stress varies appreciably through the surface layer; one feature that separates this approach from most previous two layer formulations.

From the similarity perspective provided by the scales of eq. (4.30), given a fixed surface roughness, z_o, the effect of increasing stability is analogous to increasing roughness in the Rossby-similarity treatment of the neutral PBL, i.e., the nondimensional surface speed decreases and the turning angle increases. The effect is demonstrated by Figure 15 and the explanation is straightforward: The surface roughness, which is independent of turbulence, becomes relatively larger as the physical size of turbulent eddies is inhibited by increasing buoyancy. The actual surface speed, of course, increases with more rapid melting because of reduced friction, as shown in Figure 16, which also demonstrates the reduction of PBL depth. The role of the stability parameter, η_*, becomes apparent when Figure 16 is compared with Figure 15.

For $u_* = 1$ cm s^{-1}, $\mu_* = 25$ represents a melting rate of roughly 50 cm per day, which would be considered extreme for the

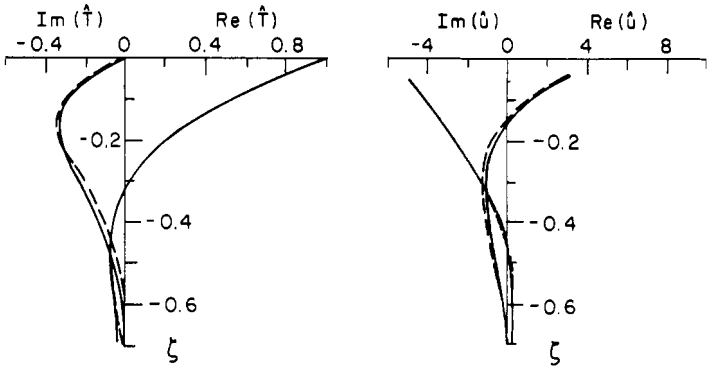

Fig. 14. Comparison of profiles from analytic similarity theory of McPhee (1981a) (solid curves) with neutral results of numerical model of Businger and Arya (1974). The profiles correspond closely even though the analytic theory uses constant K_* near the surface to calculate stress.

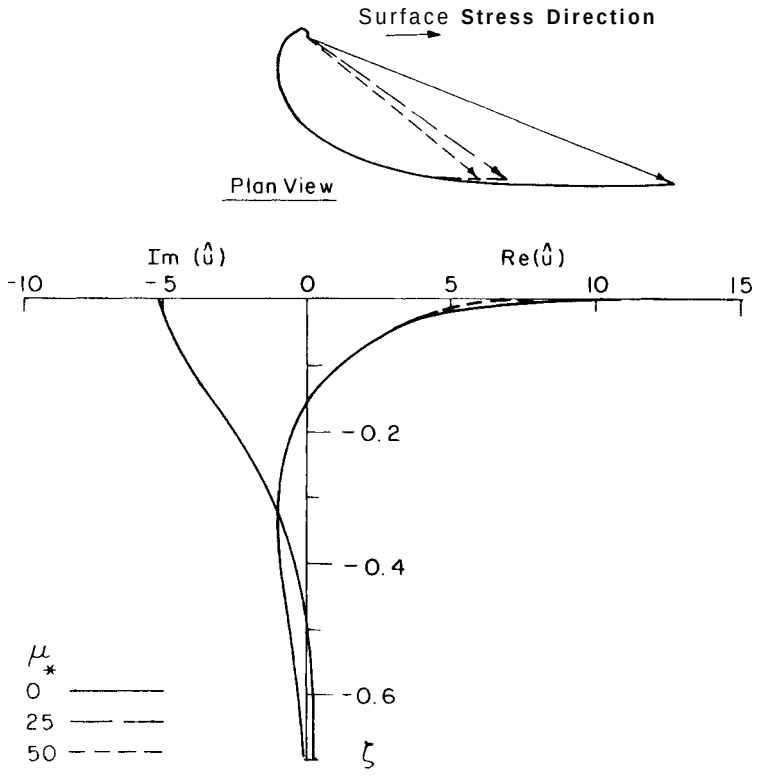

Fig. 15. Similarity velocity solutions for three values of μ_*. Other external parameters are $u_* = 1$ cm s^{-1}, $z_o = 5$ cm, $f = 1.4 \times 10^{-4}$.

interior perennial pack, but which may occasionally be encountered near the ice margin, based on observations in the Bering Sea (C. Pease, personal communication).

There are few quantitative data comparing ice drift with stress under rapid melting conditions against which to test the theory; however, the analog with the ABL can be exploited to see if the basic approach provides reasonable predictions of geostrophic drag. In the ABL geostrophic drag is often expressed in terms of the Rossby-similarity parameters A and B, thus removing explicit dependence on z_o (see, e.g., Clarke and Hess, 1974). In terms of the complex representation of surface velocity, A and B are defined by

$$B = k\ \mathrm{Im}(\hat{V}_o/\hat{u}_*) = \frac{k}{\eta_*}\ \mathrm{Im}(\hat{u}_o)$$

$$A = \ln \mathrm{Ro}_* - \frac{k}{\eta_*}\ \mathrm{Re}(\hat{u}_o)$$

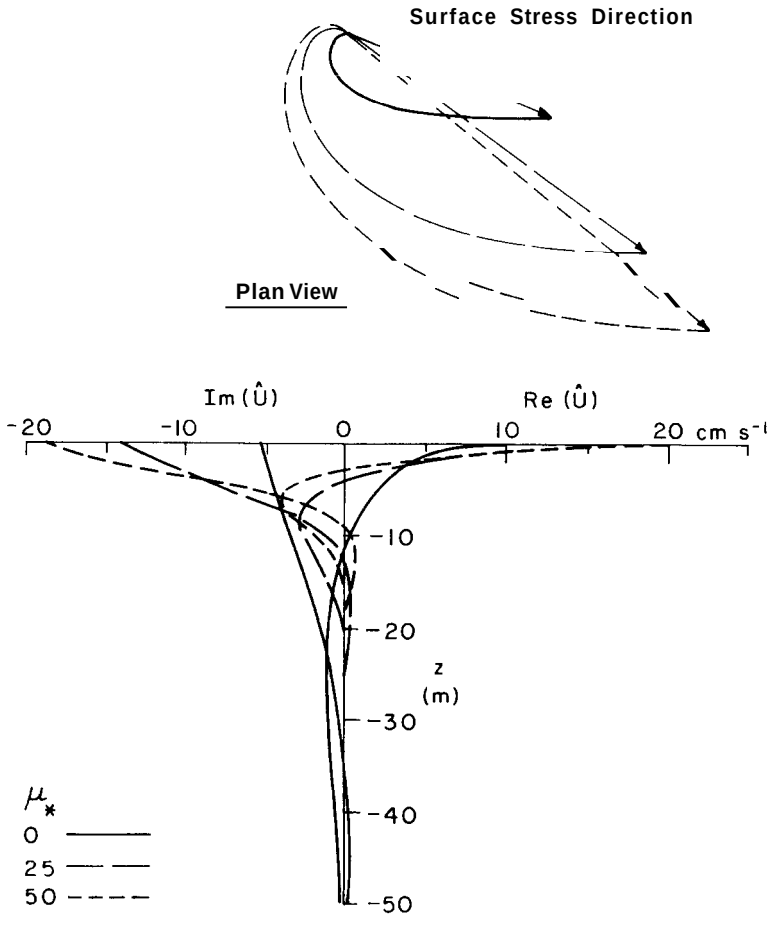

Fig. 16. Dimensional velocity components corresponding Fig. 15 where real axis is aligned with u_*.

Figure 17 shows A and B plotted as functions of $\mu_* = u_*/fL$ (the inverse of the dimensionless Obukhov length) compared with data of Clarke and Hess (1974), and with values from the models of Businger and Arya (1974), and Wyngaard (1975). The parameter curves are analytic functions; they depend only on μ_*, R_c (the critical flux Richardson number) and ξ_N, which was determined from ice drift statistics.

4.8 The Time-Dependent OBL: Inertial Oscillations

Theories of PBL momentum transfer considered so far have assumed that the inertia of the ice and upper ocean can be ignored in the force balance. In Section 2.2 it was shown, however, that drift records often contain sizable waves at the inertial period which might conceivably change the turbulent structure of the boundary layer.

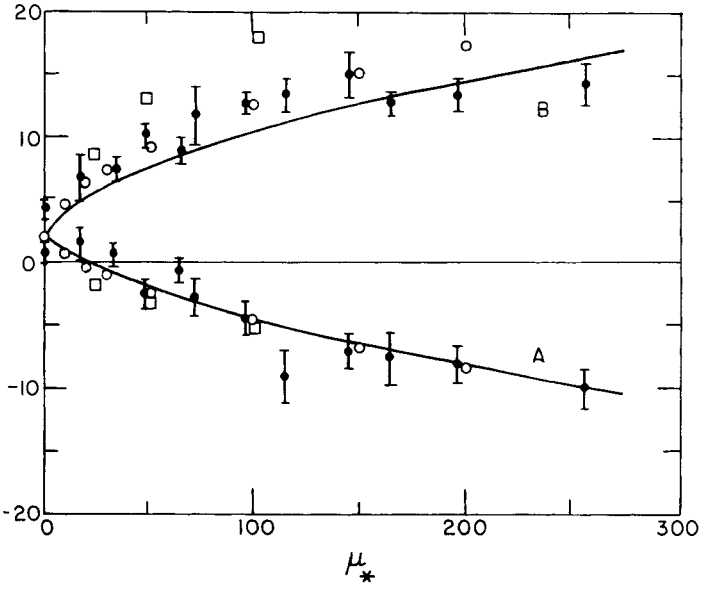

Fig. 17. The Rossby-similarity parameters A and B as functions of u_*. Solid curves are from analytic theory of McPhee (1981a); data points with error bars are from Clarke ahd Hess (1974); open circles and squares are respectively from numerical models of Businger and Arya (1974) and Wyngaard (1975).

The time-dependent nature of the PBL momentum equation was addressed by Ekman (1905, with credit to Fredholm), who presented a time varying solution for currents at various levels assuming constant eddy viscosity. Kheisin and Ivchenko (1975) extended the Ekman analysis to an ice-covered OBL.

Most simulations of observed inertial currents in the ocean have used a simpler approach (outlined in Section 2.1, see Figure 3) where mixed layer currents are related directly to transport integral, M. In most momentum integral schemes, velocity is considered uniform throughout the mixed layer, thus they are called "slab" models (e.g., Pollard and Millard, 1970). In spite of their unrealistic specification of infinite shear at the base of the mixed layer, they sometimes provide quite believable simulations of mixed layer currents. In an early analysis of AIDJEX current meter data, we used the same basic concept to simulate currents measured relative to the ice, although the mixed layer was not treated as a slab (McPhee, 1978).

In a later paper (McPhee, 1980a) a different technique was used to model observed surface velocity and upper ocean currents: The time-dependent partial differential equations for stress were solved numerically across a vertical grid using an eddy viscosity

given by eq. (4.23), with $|v_s|$ equal to 6. The dimensional eddy viscosity in the mixed layer thus depends on u_* and f as well as depth, and is assumed to adjust instantly to changing surface conditions.

Experimentation with the model showed that while the stationary part of the solution was not very sensitive to details near the base of the mixed layer, the inertial component was; in fact, nearly all of the inertial shear took place in the upper part of the pycnocline even though stress levels there were small. For this reason, the original model (i.e., similar to Businger and Arya, but with time dependence added) was modified to include a more realistic pycnocline treatment.

In the stratified fluid just below the mixed layer, the eddy viscosity is proportional to the product of a local friction velocity and the local Obukhov length:

$$K_p \propto \tau_p^{1/2} L_p = \frac{\rho_o \tau_p^2}{gk\overline{\rho' w'}|_p}$$

where the subscript, p, refers to the pycnocline near the mixed layer interface. By Reynolds analogy, we assume that the density flux is proportional to the eddy viscosity times the mean density gradient, arriving at

$$K_p = c_{pyc} \tau_p / N \tag{4.32}$$

where N is the buoyancy (Brunt-Vaisalla) frequency defined by

$$N^2 = -\frac{g}{\rho_o} \frac{\partial \rho}{\partial z}$$

and c_{pyc} is a proportionality constant that may depend on the stratifying agent (salt in the arctic pycnocline, heat in many temperate pycnoclines).

Figure 18 from McPhee (1980a) compares in the zonal component of observed and simulated surface velocity at three AIDJEX camps for the 12 day period shown in Figure 8, using $c_{pyc} = 0.20$ with a timestep of 15 minutes, and a constant mixed layer depth of 25 m. Figure 19 shows one component of velocity as simulated at three levels in the mixed layer and at one 5 m below the mixed layer, along with the average current. The inertial part of the velocity signal, which obviously dominates the low frequency part at mid-depths in the mixed layer, is fairly uniform throughout the layer. Most of the inertial shear occurs near the top of the pycnocline, which helps explain the apparent success of slab models. This suggests that the inertial and low frequency motions might be modeled independently, then combined to obtain the total velocity.

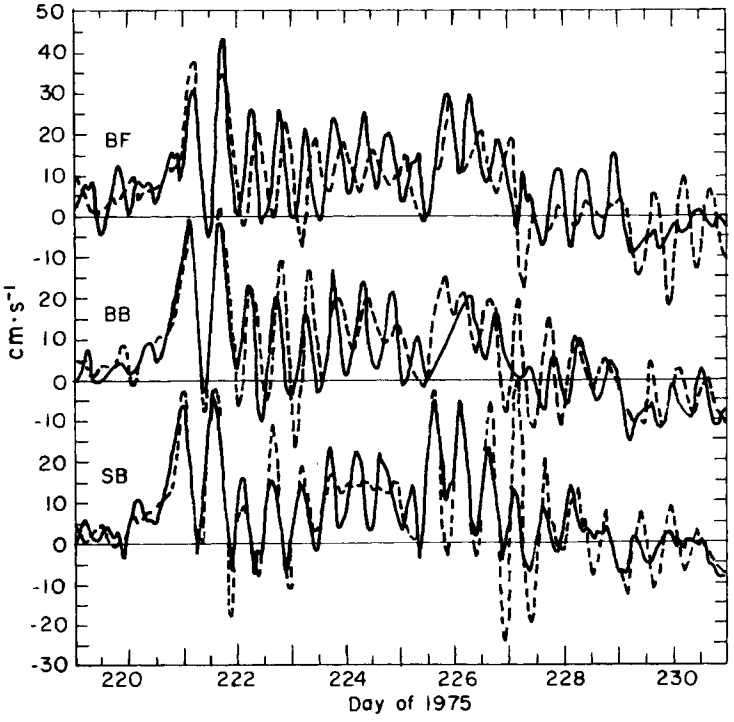

Fig. 18. Zonal component of surface velocity including inertial oscillation as observed at three AIDJEX stations (solid curves) and as simulated with model of McPhee (1980a).

The role of inertial motion in the formation and ablation of pack ice is not well understood, but could be important. During the year-long AIDJEX drift, the inertial component of ice velocity was large relative to mean drift only during a melt season that lasted about 60 days. There are probably two reasons for this: first, the mixed layer shoals because of the introduction of fresh meltwater, trapping the inertia over a smaller vertical distance; and, second, the ice pack is less capable of supporting internal stress gradients that would otherwise arrest the short period excursions. If the amplitude of inertial motion depended only on mixed layer depth, there would still be oscillations in winter about half as large as in summer; also, the transition from summer to winter conditions would be fairly gradual. Instead, the AIDJEX data showed the transition to be abrupt (it coincided with the breakup of the main station, Big Bear) and inertial amplitudes in winter to be quite small. One can thus assume that internal ice stress is mainly responsible for quelling inertial waves. This being the case, ice production could be significantly increased during the freezeup period by a mechanical pumping effect associated with the inertial motion. Ice production would be enhanced by divergences that expose areas of open water, causing more rapid cooling by sensible, latent, and radiant heat transports.

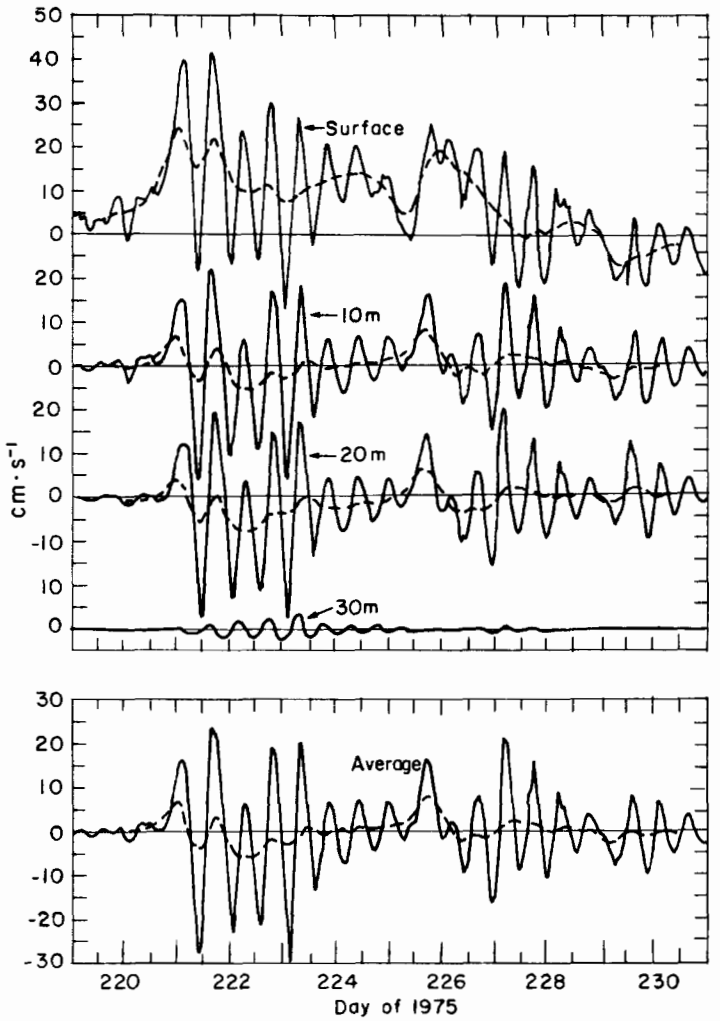

Fig. 19. Simulated velocity at three levels in mixed layer and one below, along with average velocity in the mixed layer. In the model, there is little shear in the inertial part of the velocity signal within the mixed layer.

Nansen, writing in his diary of the drift of Fram in October, 1893, described dramatic ice pressures that occurred twice daily, in between which the Fram lay in open water (see, e.g., excerpts in Manley and Lewis, 1968). Nansen thought the periodic pressures to be caused by tides, but in retrospect they seem more likely to have been the result of inertial effects as the ice tightened into its winter regime. Note that in summer, the Fram probably did drift in inertial loops, but this would have been difficult to detect without sophisticated navigation gear or continuous current measurements below the mixed layer.

In early summer, inertial waves might have the opposite effect by periodically increasing the amount of opening, which would decrease the mean albedo. In either case, the ability of the wind systems to induce inertial oscillations (e.g., sharp fronts rather than steady zonal flow) at the time of breakup or freezeup might have a decided impact on the subsequent ice characteristics.

5. DENSITY STRUCTURE OF THE UPPER OCEAN

Heat exchange across the air-ice-sea boundary is central to understanding how sea ice affects climate, and the means by which heat transfer occurs is inextricably tied to the turbulent structure of the upper ocean. The problem, of course, is not confined to high latitudes: The seasonal evolution of the upper ocean is one of the foremost problems in physical oceanography, because, among other reasons, the upper ocean is a tremendously large heat reservoir.

The polar regions differ from most of the world ocean in that heat exchange is mostly latent. If one thinks in terms of a one-dimensional system in which all the heat stored during summer is released the following winter with no net gain or loss, then for most of the perennial ice pack, the "mixed layer" problem is essentially the ice thickness distribution problem, because the upper ocean remains near its freezing point and stores little sensible heat compared with the energy that is absorbed by melting and released by freezing. In other words, if sea ice growth and decay over the seasonal cycle is well understood, a mixed layer model will add only minor corrections to the total heat budget. In this idealized view, the most important aspect of the OBL would be how the mechanical forces it exerts affect ice growth.

In reality, our knowledge of the annual ice cycle cannot be comprehensive without knowledge of the upper ocean: e.g., the temperature at which ice forms depends on mixed layer salinity. Furthermore, when low ice concentrations occur in the marginal ice zone (which includes much of the Southern Ocean about Antarctica), the upper ocean does store considerable heat, thus there are compelling reasons for studying its temperature and salinity structure.

In this section we shall briefly review some different approaches to upper ocean modeling used in the open ocean, discuss surface buoyancy and momentum flux, and outline the development of a model for predicting changes in upper ocean density during the melt season using concepts introduced in the previous section. Finally, we shall point out that one of the really interesting problems regarding oceanic heat -- namely, the fate of heat advected into the Arctic Basin from the North Atlantic -- is not amenable

to simple one-dimensional modeling, but appears instead to be an advective phenomenon involving complex exchanges in the large marginal seas of the Arctic.

5.1 Upper Ocean Models

Aside from integration of the three-dimensional, primitive flow equations (Deardorff, 1972), there are essentially two classes of models for simulating changes in salinity and temperature near the surface. In one, the differential form of the horizontally homogeneous PBL equations (eqs. 4.1-4.3) is used, with some means of closing the equations in terms of known quantities. Profiles of velocity and density are calculated at each time step. Within this category, there are numerous closure techniques including specification of a mixing length dependent on stratification (e.g., Mellor and Durbin, 1975); and "second-order" closure models in which explicit equations for the second-moment quantities (e.g., $\overline{w'T'}$) are solved along with the mean quantity equations (e.g., Wyngaard, 1975). Such models have been used to successfully simulate some oceanic conditions and provide valuable research tools, but tend to be rather complex and time consuming for use, say, in climate simulation.

In the second class of upper ocean model, properties are assumed to be uniform throughout the mixed layer and integrated forms of eqs. (4.1-4.3) are used to predict its characteristics. In these models the mixed layer depth (or its time derivative, usually called entrainment velocity) becomes a calculated variable. With many variations, mixed layer models can be broken into two subclasses. In one, exemplified by Kraus and Turner (1967), the change in mixed layer depth is calculated from an energy balance in which potential energy changes associated with surface buoyancy and entrainment of denser water from below is equal to the surface energy input plus the rate of working by surface stress less the integrated turbulent dissipation. Consider a special case of a mixed layer with no surface buoyancy and constant surface wind stress. The rate of working at the surface is proportional to the cube of the surface wind (assuming no ice), and although most of the energy derived from the wind is dissipated as turbulence, what is not goes into entraining denser water upward, increasing the potential energy of the water column and thus conserving energy. Earlier versions set aside a fixed proportion of the surface work for entrainment, thus a deep mixed layer would have as much energy available for entrainment as a shallow one, which is probably unrealistic. P. Lemke (personal communication) has applied an energy balance approach (with a linear falloff of available entrainment energy from the surface to 50 m) to the arctic mixed layer with reasonable results for the seasonal variation of mixed layer salinity and depth.

The other subclass of mixed layer models places emphasis on the integrated mean momentum equation rather than the energy equation. In the prototypic model of Pollard, Rhines, and Thompson (1973), integrating the momentum through the mixed layer leaves a stress at the base which is equated to the impulse needed to boost the momentum of the entrained fluid to the value of the mixed layer slab, i.e.,

$$\tau(z = -h) = u \frac{\partial h}{\partial t}$$

where u is the average velocity of the slab and h is its thickness. Closure is accomplished by setting a bulk Richardson number (i.e., g times the ratio of the bulk density gradient to the velocity shear squared) to unity. One obvious problem with the Pollard et al., approach is that in the steady wind, no-buoyancy-flux case, the layer deepens only during the first half-inertial period. A more fundamental criticism is that mean momentum is not uniformly distributed through the layer, particularly when it is deep, which casts doubt on many of the assumptions regarding the critical Richardson number and the entrainment mechanism. Niiler (1975) has attempted to rationalize the two different mixed layer approaches in a combined model, but the conundrums posed by ignoring mean quantity gradients within the bulk of the layer make his physical arguments for energy partition obscure, and in some ways contradictory to much recent ABL theory.

A comprehensive review of upper ocean modeling is found in the proceedings of the 1975 NATO Advanced Study Institute, "Modelling and Prediction of the Upper Layers of the Ocean" (Kraus, 1977). It is perhaps obvious from the previous sections that (in the author's view) turbulence in the OBL under pack ice should be treated explicitly using eddy diffusivity concepts. Below we shall show how the analytic similarity theory can be extended to include buoyancy flux at the base of the mixed layer. The method requires relatively little computation but retains many of the physical concepts suggested by the AIDJEX OBL measurements.

5.2 Buoyancy at the Ice/Ocean Interface

Just as the summer AIDJEX measurements provided a rare opportunity to test the relationship between surface stress and velocity, they also represent a rather special data set for testing upper ocean density models, since they include daily STD (salinity-temperature-depth) profiles. By monitoring the change in salinity of the upper layers, the surface buoyancy flux can be estimated. When combined with accurate stress estimates, this provides a set of forcing functions hard to duplicate with measurements from the open ocean.

Figure 20 shows salinity and temperature of the upper 200 m of the ocean measured at AIDJEX station Snowbird on days 169, 198, and 227 of 1975. The first case is representative of late winter conditions: The mixed layer is nearly uniform to about 52 m and close to its freezing point. The second shows development of a step-like structure as fresh meltwater is introduced and mixed to varying depths. The third cast was taken near the time of maximum accumulated meltwater. Note that the mixed layer is only about half as deep, is much fresher, and has warmed slightly.

Over the course of the melt season the stations drifted about 200 km to the southeast, so that advective change in the water column must be considered. From looking at spatial variation in the profiles, it was clear that horizontal gradients in density were present, especially in one rather narrow zone through which all the camps passed. However, by looking at the shapes of the profiles, and by comparing data from drift tracks that traversed the same regions at different times, we found that at depths of about 40 m, the salinity profiles were not affected by surface conditions, even though the absolute salinity value might change with position. Thus, by assuming the value of salinity measured at 40 m at each location represented the mixed layer value there when the melt season began, we were able to calculate the cumulative salinity flux for that cast. Since the source of the negative salinity flux was melting ice (neglecting precipitation), an ablation curve for the pack can be constructed from the salinity

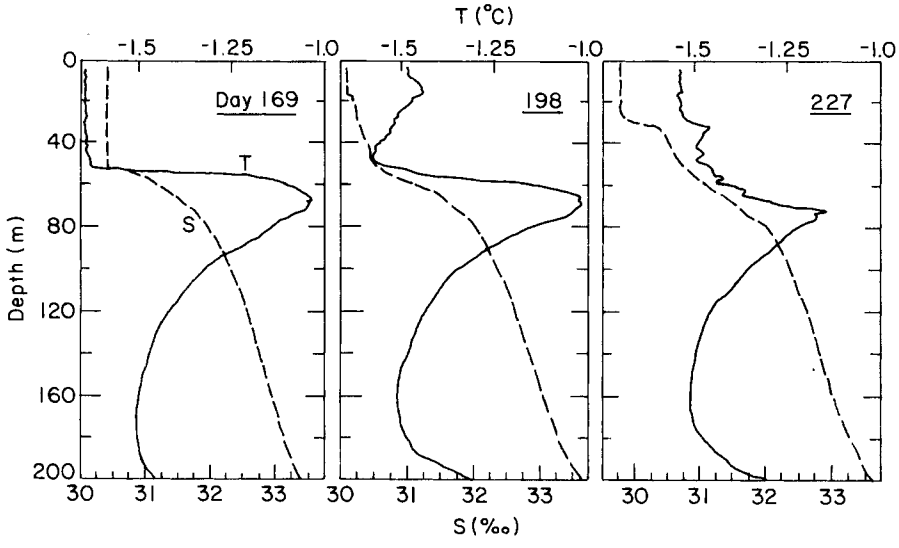

Fig. 20. Salinity and temperature measured at AIDJEX station Snowbird, Summer 1975.

measurements; i.e., for each cast the change in ice thickness from the start of the melt season is given by

$$\delta H = \frac{\rho_w}{\rho_{ice}} \cdot \frac{(\bar{S} - S_{40})h}{\Delta S}$$

where h is the mixed layer depth, $\bar{S}$ is the average salinity above 40 m, S_{40} is the salinity at 40 m, and S is the salinity difference between the mixed layer and sea ice (~25°/oo). Figure 21 shows ice ablation determined this way from the STD data. The solid curve is a simple sinusoid

$$\delta H = 0.70 \quad [1 - \cos(\frac{t - 171}{90})\pi] \text{ m} \quad . \qquad (4.33)$$

The dashed curve is the basin average ablation due to thermodynamic forcing from the sea-ice model of Hibler (1980). The amplitudes are quite similar. A plausible explanation for at least part of the time lag (about 20 days) is that it takes that long for meltwater collecting at the surface to drain through and enter the main oceanic water column.

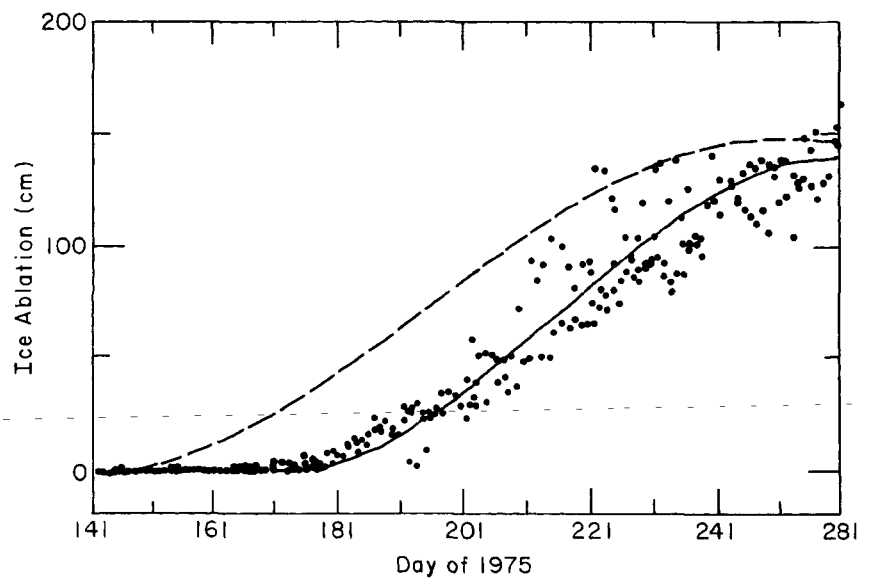

Fig. 21. Ice ablation inferred from changes in salinity of the upper 40 m at AIDJEX stations, Summer 1975 (solid line). Basin-wide, thermodynamic ablation rate from Hibler's (1980) sea ice model (dashed line).

The ablation curve eq. (4.33) can be differentiated to provide a growth rate curve which is then used to estimate the buoyancy flux as a function of time over the region in which the camps drifted.

5.3 An Upper Ocean Model Based on the Stress Equation

With time series of stress and buoyancy at the surface it seems reasonable to try a simulation of upper ocean density evolution during the melt season using most of the conceptual tools developed for the underice OBL from previous work. Here we present a previously unpublished model which represents a preliminary attempt based on an extension of the similarity theory of McPhee (1981a). It is predicated on the following assumptions.

1. Time-dependent (inertial) terms may be ignored in the turbulent stress equation, so that the stress profile is always in equilibrium with the interfacial stress at the surface.

2. Mixing of scalar properties (specifically, Θ and S) occurs to a limiting depth: $z_{dyn} = \zeta_{max} \eta_* u_*/f$, unless the depth of the pycnocline is less than z_{dyn}. This is a restatement of the familiar idea that there is a limiting depth to which turbulence penetrates in a neutrally stratified, rotating boundary layer.

Consider a stratified ocean topped by a well mixed (neutrally buoyant) layer, with surface fluxes of momentum and buoyancy (which is zero or positive). Two conditions will cause the initial density structure to change. In the first case, positive buoyancy dominates and the lighter fluid introduced at the surface mixes downward to some level higher than the original mixed layer depth so that as time progresses, a lighter, shallower mixed layer forms. Our assumption is that the depth of this new layer is given in the similarity vertical coordinate by ζ_{max}. This behavior is already implicit in the similarity theory so long as ζ_{max} is specified.

In the second case, the interfacial stress is strong enough to cause an upward flux (entrainment) of denser fluid at the base of the pre-existing mixed layer, even though there is no negative (unstable) surface buoyancy. If conditions remain steady, this flux will densify the mixed layer and it will deepen along the underlying density gradient until it reaches the depth z_{dyn}. In order to quantify this tendency, we need an expression for the flux of momentum and buoyancy at the mixed layer/pycnocline interface.

When the nondimensional pycnocline depth, ζ_p, is shallower than ζ_{max}, we have a situation like that sketched in Figure 22 where there is a finite stress and turbulent mixing at the level,

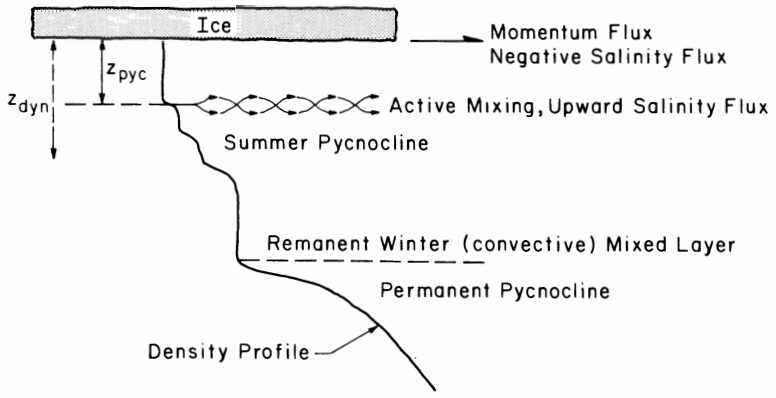

Fig. 22. Schematic of the upper ocean regime during the summer melt season.

ζ_p. In the upper (mixed) layer, the eddy viscosity is given by K_{*m} and below ζ_p we assumed that it has a small, depth-independent value, K_{*p}. The nondimensional stress equation is

$$\frac{i\hat{T}}{K_*} = \frac{\partial^2 \hat{T}}{\partial \zeta 2} \tag{4.34}$$

with boundary conditions $\hat{T}(0) = 1$, $\hat{T}(-\infty) = 0$. In the mixed layer the solution is

$$\hat{T} = \hat{A}e^{\hat{\delta}\zeta} + \hat{B}e^{-\hat{\delta}\zeta}$$

where $\hat{\delta} = (i/K_{*m})^{1/2}$. Since $\hat{T}(0) = 1$, we have

$$\hat{T}(\zeta) = 2\hat{A} \sinh\hat{\delta}\zeta + e^{-\delta\zeta} \; ; \quad \zeta \geq \zeta_p$$

and

$$\hat{v}(\zeta) = -i \frac{\partial \hat{T}}{\partial \zeta} = -i\hat{\delta}(2\hat{A} \cosh \hat{\delta}\, \zeta - e^{-\hat{\delta}\zeta})$$

away from the thin surface layer.

In the lower stratified layer the solution to eq. (4.32) is

$$\hat{T} = \hat{C}e^{\hat{\gamma}\zeta}$$

where $\hat{\gamma} = (i/K_{*p})^{1/2}$ since $\hat{T}(-\infty) = 0$. At $\zeta = \zeta_p$,

$$\hat{T}_p = 2\hat{A} \sinh \hat{\delta}\zeta_p + e^{-\hat{\delta}\zeta_p} = \hat{C}e^{\hat{\gamma}\zeta_p}$$

whence

$$\hat{T}(\zeta) = \hat{T}_p e^{\hat{\gamma}(\zeta - \zeta_p)} \quad ; \quad \zeta < \zeta_p$$

and

$$\hat{V}(\zeta) = -i\hat{\gamma}\hat{T}_p e^{\hat{\gamma}(\zeta - \zeta_p)} \quad .$$

By matching velocities at ζ_p, $\hat{A}$ can be eliminated. In the mixed layer $K_{*m} = k\xi_N$, which is known, but in order to close the problem, an expression for K_{*p} is required. It is obtained in the same way as the expression for eddy viscosity in the time-dependent model, eq. (4.3). At the outset, the stress at the pycnocline interface, $\hat{T}_p u_* \hat{u}_*$, is unknown so the algebraic equation is implicit and is solved iteratively. Once $\hat{T}_p$ is known, the stress distribution is known, and by Reynolds analogy the flux is determined given the ratio K_ρ/K. In this way the buoyancy flux at the base of the mixed layer is calculated from surface conditions and is used along with the surface buoyancy in determining the evolution of the density structure.

Figure 23 compares the density structure predicted by the model outlined above every 5 days for a 70-day period at AIDJEX Station Snowbird. In this run the ratio K_s/K was 0.1 and the nondimensional maximum mixing depth was $\zeta_{max} = 0.4$. In the model, surface forcing is never strong enough to change the density profile below about 35 m, so for comparison, the observed profiles are forced to match the model at the 40 m level. The numbers there indicate the observed change in density (σ_t units) from the initial value on day 170, and probably represent the advective change as the ice drifted southeast.

The series of steps produced by the model result when the maximum depth of mixing ($\zeta_{max}\eta_* u_*/f$) is less than the existing mixed-layer depth, so that fresh water introduced at the surface is trapped within that layer. The effect of turbulent stirring set up by rapid ice motion is clearly demonstrated by the deepening of the mixed layer from days 210 to 225. During this time the stabilizing surface buoyancy flux is near its seasonal maximum, so that the deepening must result from shear-generated turbulence.

It is not surprising that the steps in the model profiles are more abrupt than in the observations. First, other processes like energy leakage from internal waves and molecular diffusion act to destroy sharp gradients. Perhaps more important is that turbulent mixing is intermittent and would tend to feather out more gradually

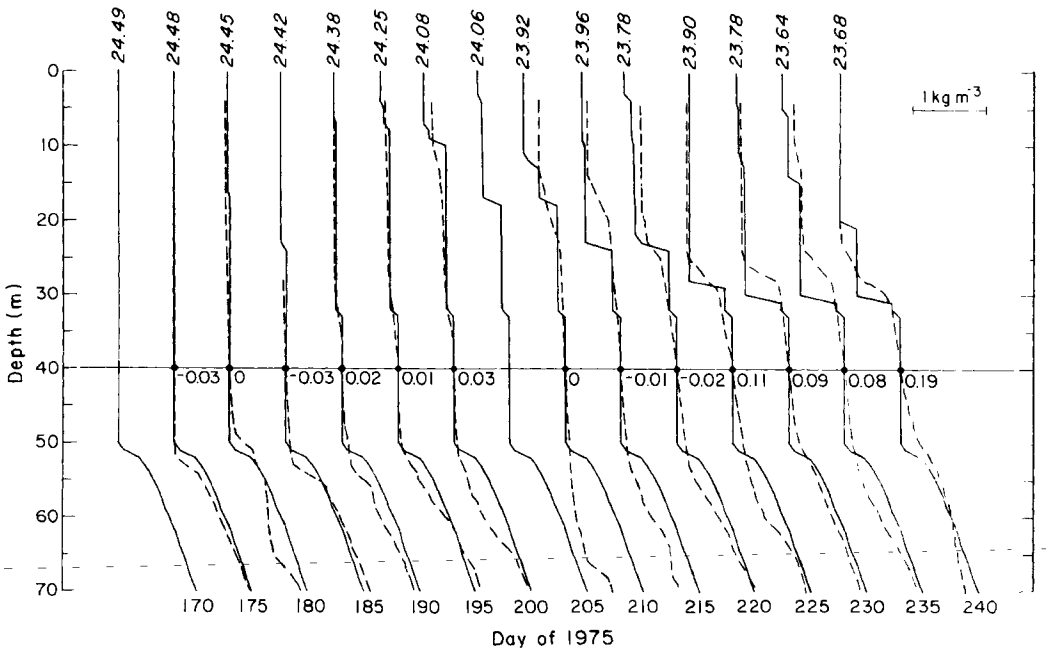

Fig. 23. Comparison of modeled (solid) and observed (dashed) density profiles at AIDJEX station Snowbird, Summer 1975.

than the abrupt limit specified in the model. Nevertheless, it is worth noting that of several values tried, $\zeta_{max} = 0.4$ does the best job of describing the formation of the lighter layers. In the limit $\eta_* \to 1$ (no surface buoyancy) this is consistent with the notion that the limiting depth of the neutral PBL is about ku_*/f.

The model is still in the developmental stage, but results so far are encouraging. Unlike the "slab" mixed-layer models, it also furnishes reasonable estimates of currents at all levels, including the surface (ice), as long as z_o is known.

6. THE UPPER OCEAN IN THE MARGINAL ICE ZONE

The Marginal Ice Zone (MIZ), where the ice concentration falls rapidly at the edge of the ice pack, may contain some of the most complex upper-ocean structure found anywhere; mainly because the ice can induce extreme gradients in surface heat and salt flux, and can change surface drag characteristics. Since ice is an efficient insulator, the atmosphere over the interior pack can reach temperatures far below those normally encountered in maritime regimes. When this cold air is advected over open water the temperature contrast is large, with correspondingly large latent and sensible heat flux. In summer, the albedo contrast between

ice and open water is also great, so that net radiation influx can vary rapidly across the MIZ, although this effect may often be ameliorated by cloudiness.

A feature commonly observed across the MIZ is an abrupt change in mixed-layer temperature, during winter as well as summer, indicating the importance of advective processes in the ocean (otherwise near-surface temperatures would be uniformly near freezing). Observations (e.g., Pease, 1980) have shown that even thick ice melts rapidly when advected into the warmer water, thus the small-scale exchange of heat and salt between ice and warmer water is an important component in addressing the overall flux budgets.

The similarity theory described earlier (McPhee, 1981) predicts, for example, that surface drag characteristics will change appreciably under such conditions. In addition, surface buoyancy should have large impact on OBL currents and transport, as demonstrated in Figure 16. Consider a hypothetical situation in which initially a sharp front in mixed-layer temperature exists at the ice margin. Now impose an off-ice wind stress that produces a boundary layer under the interior pack (where there is no melting) like that depicted in Figure 16 for $\mu_* = 0$; and for the sake of argument assume that the temperature difference across the front is sufficient to cause the melting required for $\mu_* = 25$ on the seaward side of the front. According to the theory, the whole pack should move down-wind with some rightward deflection, but ice at the leading edge will encounter less drag and will thus separate from the main pack with a slight additional rightward deflection. Note also that water in the top few meters of the boundary layer will follow the ice with a downwind (real) component, tending to insulate ice following the leading edge from intense melting. Without buoyancy flux, the trailing ice will not experience a drag reduction; therefore, fairly rapid development of a polynya behind the leading ice edge can be expected.

In the water column, mean shear will rapidly smear the sharp front that existed initially. An interesting convergence is implied by the PBL dynamics: back under the interior ice, there is a net transport toward open water in the layer from about 3 to 12 m which is compensated by opposite transport below (geostrophic departure requires the real component of velocity to integrate to zero over the whole column). Under ice that is rapidly melting, however, there is an appreciable current opposite to the wind stress throughout the same layer (in the atmosphere, the analog is called the nocturnal jet). This current would advect warm water back toward the interior, at some point meeting cold water advected by the neutral OBL; the resulting convergence could then force warm water back toward the surface where it would again interact with the ice. Effects like this might account, at least in part,

for extensive finestructure in temperature observations from the MIZ (Paquette and Bourke, 1979); and for the tendency of the ice to form periodic bands parallel to the ice edge under the influence of off-ice winds. Wadhams (Chapter 15) has developed an alternative theory for band formation which involves wave-radiation stress imparting additional momentum to floes at the margin. His approach would obviate the requirement of rapid melting for band formation.

An interesting consequence of large horizontal flux gradients at the MIZ is the potential for oceanic circulations with scales larger than those of the boundary-layer processes, but still much smaller than permanent oceanic features. An obvious example occurs if the ice edge is stationary, like a glacial shelf or fast-ice boundary, in which case the abrupt change in transmission of wind stress to the water column is analogous to a coastal upwelling regime. Details of circulation that might ensue have been investigated by Gammelsrod, Mork, and Roed (1975) and by Clark (1977). The main effect is that in situations where OBL transport is away from the ice (e.g., a westerly wind with ice poleward), an appreciable upwelling can occur at the ice edge. If warmer water is to be found at depth, this represents a mechanism by which heat exchange between ocean and atmosphere might be enhanced. If the ice cover is drifting freely, this mechanism is much less dramatic because the ice, as it moves, transmits a large proportion of the wind stress to the ocean.

Buckley et al. (1979) reported evidence for upwelling near a well-defined, but apparently freely drifting, ice edge north of Spitzbergen, which they attributed to a sharp wind stress gradient during an intense storm that had traversed the region a few days prior to the time of their observations. McPhee (1980c) speculated that a different mechanism, more closely akin to a sea-breeze cell than coastal upwelling, could have induced the structure observed by Buckley et al. (1979). The basics of the argument, which is at best a crude approximation of a real situation, are presented below. It is fashioned closely on a similar exposition of sea-breeze circulation in the atmosphere by Holton (1972, Chapter 5).

Starting from the fundamental circulation theorem, which states that the time rate of change of absolute circulation about a closed loop of fluid particles is equal to the line integral of the so-called solenoidal term; we have:

---

[1]It was pointed out during discussion at Maratea that the description pertaining to Figure 13 of McPhee (1980c) wrongly labels isosteric (constant specific volume) surfaces as isopycnal. The inferred circulation remains as shown.

$$\frac{d\bar{C}_a}{dt} = -\oint \frac{dp}{\rho}$$

This is applied to the system sketched in Figure 24. Consider a 50 m deep mixed layer that is densified by about 0.1 kg m^{-3} relative to the mixed layer under the ice (this represents combined ice growth and evaporation of roughly 20 cm). Proceeding clockwise about the circuit drawn, the integral is approximated by

$$\oint \frac{dp}{\rho} \simeq \Delta P \left(\frac{1}{\bar{\rho}} + \frac{1}{\bar{\rho} + \delta\rho}\right) \simeq \frac{\Delta P\ \delta\rho}{\bar{\rho}^2}$$

where a Taylor's series expansion is used to estimate the second factor. With $\Delta P = 5 \times 10^5$ Pa, and $\delta\rho = 0.1$ kg m^{-3}, the time rate of change of mean absolute circulation is

$$\frac{d\bar{C}_a}{dt} = 0.05\ m^2 s^{-2}$$

This implies an appreciable acceleration in the mean velocity about the circuit if no other factors affect the flow, i.e.,

$$\frac{d\bar{V}}{dt} = \frac{1}{2(H+L)} \frac{d\bar{C}_a}{dt} \quad 1.25 \times 10^{-6} ms^{-2}$$

which would amount to an increase in the clockwise velocity component of roughly 10 cm s^{-1} over a day. It is clear, however, that rotational and frictional dissipation effects would soon come into play that would completely distort this oversimplified view -- it is in fact the frictional forces that could give rise to upwelling, although probably not of the magnitude reported by Buckley et

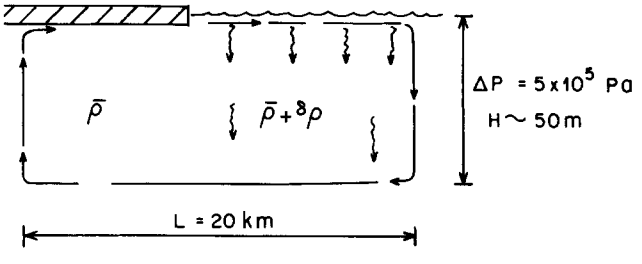

Fig. 24. Schematic of circulation cell resulting from sharp gradient in surface buoyancy flux at the ice margin. The line integral of the solenoidal term is evaluated about the circuit shown.

al. (1979). In terms of a mechanism for extensive upwelling at the ice edge, this approach suffers the same drawback as the stress-gradient proposal: namely, that the ice is mobile, and would in most circumstances move in response to the same forcing as the water, thus tending to smear out the sharp gradients in surface forcing. Røed (personal communication) has begun development of a more sophisticated combined ice-ocean model for the MIZ that shows promise of providing better understanding of these complex phenomena.

On a geophysical scale, freezing is one of the most effective distillation processes. The occurrence of sharp horizontal density gradients in the upper ocean that may result from differential freezing leads naturally to a classic problem in rotational fluid dynamics: geostrophic adjustment. Rossby (1938) was the first to explore theoretically how a region of anomalous density adjusts with surrounding fluid in a rotating system. Stern (1975, Chapter 3) treats the collapse of a lens of intermediate density water released suddenly between two stratified layers, as sketched in Figure 25. In brief outline, Stern's argument is as follows. If the fluid is assumed inviscid, Euler's equation for the intermediate lens can be written in terms of the "reduced gravity" as

$$\frac{d\underset{\sim}{V}}{dt} + f\,\hat{k} \times \underset{\sim}{V} = -g_* \nabla h$$

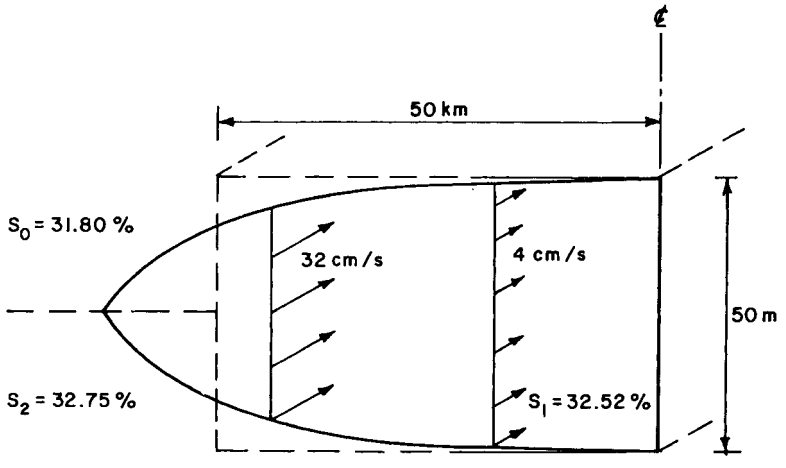

Fig. 25. Limited collapse of lens of intermediate density fluid with initial thickness 50 m, half-width 50 km, between layers in a rotating, inviscid fluid. Adapted from Stern (1975).

where h is the thickness of the lens and g_* is the reduced gravity:

$$g_* = g \left(\frac{\rho_1 - \rho_0}{\rho_1}\right) \left(\frac{\rho_2 - \rho_1}{\rho_2 - \rho_0}\right)$$

when ρ_0, ρ_1, and ρ_2 are respectively the densities of the upper, intermediate, and lower layers. Let ζ be the vertical component of local vorticity. If it is assumed that in the intermediate layer of depth, h, the horizontal velocity is independent of depth, then

$$\frac{d}{dt}\left(\frac{\zeta+f}{h}\right) = 0$$

which states that potential vorticity $(\zeta+f)/h$, is conserved. In the initial state, the fluid is at rest with potential vorticity, f/h_0. In the final state, it will achieve geostrophic balance, so that the pressure gradient within the slumping lens is in equilibrium with the Coriolis force, i.e.

$$fv = g_* \frac{\partial h}{\partial x}$$

where v is the velocity component along the lens axis. Since potential vorticity is conserved, the final lens thickness is described by the equation

$$f + \frac{g_*}{f} \frac{d^2h}{dx^2} = \frac{fh}{h_0}$$

with solution

$$h = h_0 \left(1 - \frac{\cosh \frac{(x/\lambda_R)}{}}{\cosh (L/\lambda_R)}\right)$$

where

$$\lambda_R = \sqrt{\frac{g_* h_0}{f}}$$

is the Rossby radius of deformation. Conservation of mass provides an expression for the final length of the lens:

$$\frac{}{\lambda_R} - \tanh \frac{L}{\lambda_R} = \frac{L_0}{\lambda_R}$$

If λ_R is small compared to L_0, the lens spreads a comparatively small distance before reaching equilibrium; and, in the absence of any dissipation would remain in motion parallel to its long axis indefinitely. In reality, turbulent dissipation would slow currents near the nose, and the feature would migrate farther into the two-layer regime as it lost potential energy.

Figure 25 shows the ideal solution for intrusion of a lens of water with salinity 32.52°/oo between layers with salinity 31.80°/oo and 32.75°/oo. For these values the Rossby radius is about 12 km; the idealized solution shows. that the final state departs noticeably from its initial configuration only within about two deformation radii from the nose. Note also the current parallel to the lens axis, increasing toward the nose.

The specific parameters of Figure 25 were chosen to coincide with measurements made during a helicopter survey of upper ocean CTD structure near the drift station FRAM I in April, 1979, described in more detail by McPhee, 1980d. During' the course of the survey, which spanned about 6 weeks, we found a dramatic change in mixed layer characteristics throughout the survey region despite generally mild winds. The mixed layer to the east was deeper and markedly more saline than it was in the area directly west of camp; the change occurred across a narrow frontal region which meandered roughly north-south as far as we could sample. Fortuitously, the camp itself drifted over the frontal zone. Near the center, profiling current meter casts showed little or no current above about 15 m; then a strong shear between 15 and 20 m marking the upper boundary of a mostly unidirectional (current toward the northwest) jet with speeds of about 10 cm s^{-1} down to another shear layer from 50 to 70 m. Below this, currents were small and variable. Reasoning that the feature was in approximate geostrophic balance, we ran a survey line of helicopter casts perpendicular to the current direction. Salinity and temperature profiles for 7 casts in the linear transect are shown in Figures 26 and 27. Qualitative agreement with the inviscid geostrophic adjustment model is apparent; turbulent dissipation would obviously slow the currents and blunt the nose. The distance across which the two different mixed-layer regimes interact is about two Rossby deformation radii.

The origin of the denser water in Figure 26 is not known. We speculated that it had migrated (ageostrophically) from the shelves north of Svalbard where it had formed by intense freezing, maintained by continual offshore advection of ice. Whatever the origin, understanding the physics and thermodynamics of features like this is probably an important key to understanding the Marginal Ice Zone.

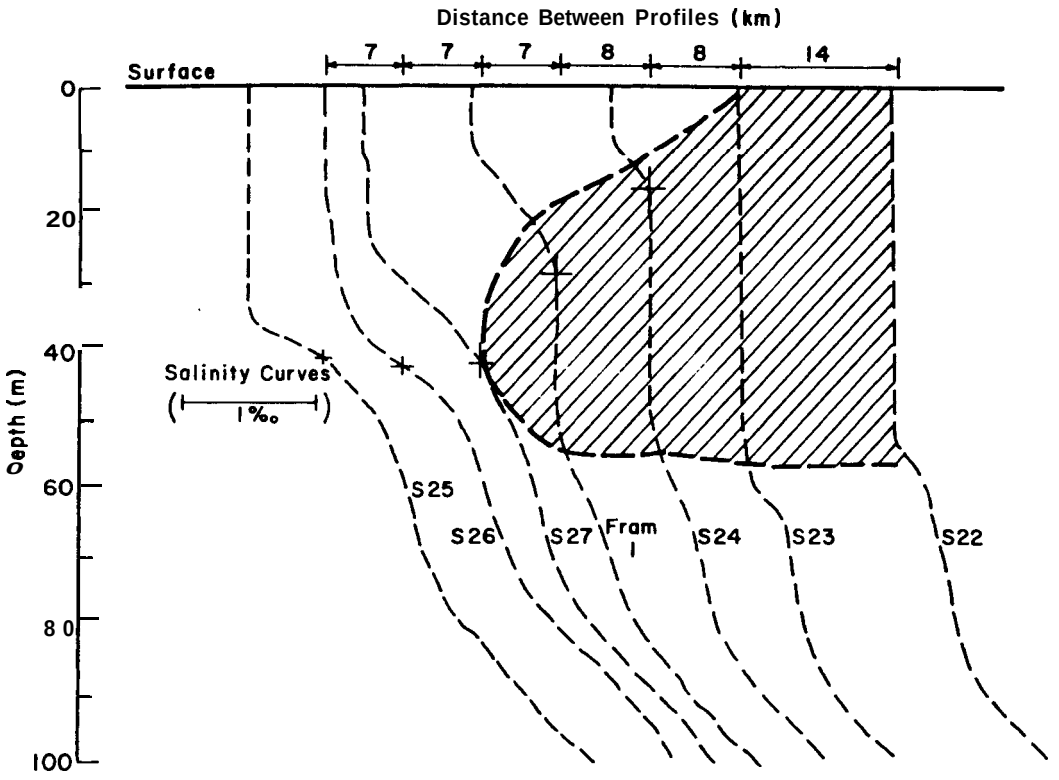

Fig. 26. Salinity profiles centered at ice station FRAM I showing intrusive layer of water with salinity 32.52°/oo. Pluses mark salinity 32.5°/oo. Samples were made by helicopter in a line perpendicular to current jet observed in a layer from 20–50 m deep at the manned station.

7. SUMMARY

Understanding of the upper ocean in contact with sea ice has increased dramatically with analysis of data from major experiments performed in the Arctic, and as general knowledge of turbulent boundary-layer processes has increased. The main thrust of the present chapter has been to show that a comparatively simply approach to parameterizing PBL turbulence, one developed primarily for the atmosphere, is an effective tool for describing and predicting characteristics of the oceanic PBL, even for phenomena such as inertial oscillations, which are not a prominent feature in the atmosphere.

Prediction of sea-ice motion requires knowledge of momentum flux at the ice undersurface. AIDJEX results have shown convincingly that drag in the interior ice pack can be described by laws analogous to atmospheric geostrophic drag laws. Equation (4.31)

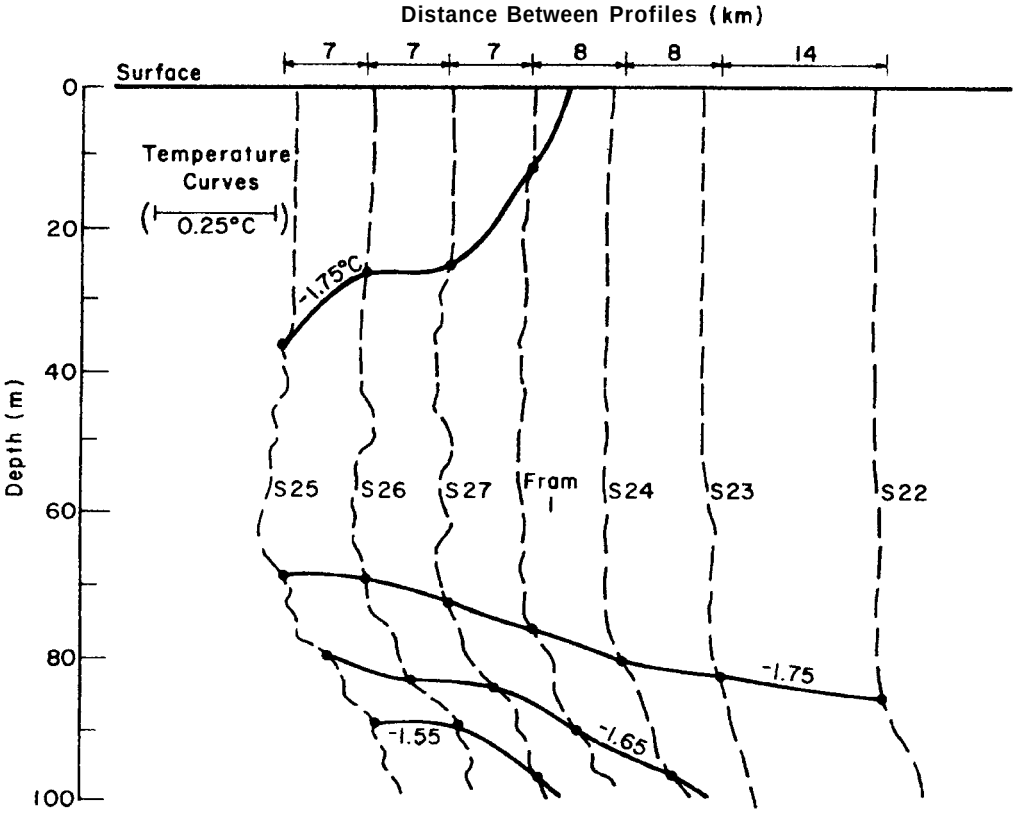

Fig. 27. Temperature profiles as in Figure 26.

represents a general statement of the drag law for sea ice. Under all but extreme circumstances, the OBL can be treated as neutrally buoyant so that $\eta_* = 1$ and $a = 0$. The main uncertainty then is how z_0 varies spatially and seasonally. Near the ice margins where rapid melting and freezing can modify turbulent structure, there is still much theoretical and observational work needed. In shallow waters, the effect of the bottom on ORL turbulence and mean velocity needs more investigation, especially when the water-column stratification is weak.

Inertial oscillations in the sea ice and underlying boundary layer are often present, especially during the melt season, partly because then the pycnocline is shallower, thus trapping the inertia in a smaller layer; but mostly because the ice is too weak to provide much damping. Their main source is rapid change in wind stress, but AIDJEX measurements indicated a coupling in the oscillations observed across the entire array (190 km) beyond that provided by the local surface winds.

Changes in density structure in the OBL caused by melting and freezing of sea ice are similar to the seasonal changes in mixed-layer characteristics observed in open oceans, except that heat exchange is mostly latent. Principles governing the physics of turbulent momentum exchange as inferred from drift characteristics can also be applied directly to estimating heat and salinity flux; a model along these lines has been successfully tested on the AIDJEX melt season data.

The potential for extreme gradients in momentum and buoyancy flux across the Marginal Ice Zone is an important factor in determining realistic estimates for air-sea exchange at high latitudes. At this'point, both our theoretical and observational bases for understanding these complex effects are limited, and the problems are challenging. Nevertheless, there is a promise that the next few years will see decided improvement, if the discussions at Maratea were any indication.

REFERENCES

Blackadar, A. K., and H. Tennekes (1968) Asymptotic similarity in neutral planetary boundary layers. J. Atmos. Sci., 25: 1015-1019.

Buckley, J. R., T. Gammelsrod, J. A. Johannessen, O. M. Johannessen and L. P. Røed (1979) Upwelling: Oceanic structure at the edge of the arctic icepack in winter. Science, 203: 165-167.

Businger, J. A. and S. P. S. Arya (1974) The height of the mixed layer in the stably stratified planetary boundary layer. In Advances in Geophysics, 18A, Academic Press, New York, p. 73-91.

Clarke, A. J. (1977) On wind-driven quasi-geostrophic water movements near fast-ice edges. Unpublished manuscript. Ocean Modelling, 8: 9-11.

Clark, R. H. and G. D. Hess (1974) Geostrophic departure and the functions A and B of Rossby-number similarity theory. Bound.-Layer Met., 7: 267-287.

Deardorff, J. W. (1972) Numerical investigation of neutral and unstable planetary boundary layers. J. Atmos. Sci., 29: 91-115.

Ekman, V. W. (1905) On the influence of the earth's rotation on ocean currents. Ark. Mat. Astron. Fys., 2: 1-52.

Gammelsrod, R., M. Mork and L. P. Røed (1975) Upwelling possibilities at an ice edge: Homogeneous model. Mar. Sci. Comm., 1: 115-145.

Hibler, W. D., III (1979) A dynamic thermodynamic sea ice model. J. Phys. Oceanogr., 9(4): 815-846.

Hinze, J. 0. (1975) Turbulence. McGraw-Hill, New York, Second Edition, 790 p.

Holton, J. R. (1972) An Introduction to Dynamic Meteorology. Academic Press, New York, 319 p.

Hunkins, K. (1967) Inertial oscillations of Fletcher's Ice Island (T-3). J. Geophys. Res., 72: 1165-1174.

Kheisin, D. Ye. and V. O. Ivchenko (1975) Water stress determination in the purely wind-induced drift. Arkt. Antarkt. Nauch. Issled. Inst., 332.

Kraus, E. (Ed.) (1977) Modelling and Prediction of the Upper Layers of the Ocean. Pergamon Press, Oxford, 325 p.

Kraus, E. G. and J. S. Turner (1967) A one-dimensional model of the seasonal thermocline. II: The general theory and its consequences. Tellus, 19: 98-106.

Manley, S. and G. Lewis (Eds.) (1968) Polar Secrets: A Treasury of the Arctic and Antarctic. Doubleday, New York, 222 p.

McPhee, M. G. (1978) A simulation of inertial oscillation in drifting pack ice. Dyn. Atmos. Oceans, 2: 107-122.

McPhee, M. G. (1979) The effect of the oceanic boundary layer on the mean drift of pack ice: Application of a simple model. J. Phys. Oceanogr., 9: 388-400.

McPhee, M. G. (1980a) A study of oceanic boundary-layer characteristics including inertial oscillation at three drifting stations in the Arctic Ocean. J. Phys. Oceanogr., 10: 870-884.

McPhee, M. G. (1980b) An analysis of pack ice drift in summer. In Sea Ice Processes and Models (R. S. Pritchard, Ed.), University of Washington Press, Seattle, Washington, p 62-75.

McPhee, M. G. (1980c) Physical oceanography of the seasonal sea ice zone. Cold Reg. Sci. Tech., 2: 93-118.

McPhee, M. G. (1980d) Heat transfer across the salinity-stabilized pycnocline of the Arctic Ocean. In Second International Symposium on Stratified Flows (T. Carstens and T. McClimans, Eds.), Tapir Press, Trondheim, Norway, p. 527-537.

McPhee, M. G. (1981) An analytic similarity theory for the planetary boundary layer stabilized by surface buoyancy. Bound.-Layer Met., 21: 325-339.

McPhee, M. G. (1982) Sea ice drag laws and simple boundary layer concepts including application to rapid melting. USA Cold Regions Research and Engineering Laboratory, CRREL Report 82-4.

McPhee, M. G. and J. D. Smith (1976) Measurements of the turbulent boundary layer under pack ice. J. Phys. Oceanogr., 6: 696-711.

Mellor, G. L. and T. Yamada (1974) A hierarchy of turbulence closure models for planetary boundary layers. J. Atmos. Sci., 31: 1791-1806.

Mellor, G. L. and P. A. Durbin (1975) The structure and dynamics of the ocean surface mixed layer. J. Phys. Oceanogr., 5: 718-728.

Neshyba, S., V. T. Neal and W. Denner (1971) Temperature and conductivity measurements under Ice Island T-3. J. Geophys. Res., 76: 8107-8120.

Neumann, G. and W. J. Pierson, Jr. (1966) Principles and Physical Oceanography. Prentice-Hall, Englewood Cliffs, N.J., 545 p.

Newton, J. L. (1973) The Canada Basin: Mean circulation and intermediate scale flow features. University of Washington, Ph.D. thesis, 158 p.

Niiler, P. P. (1975) Deepening of the wind-mixed layer. J. Mar. Res., 33: 405-433.

Paquette, R. G. and R. H. Bourke (1979) Finestructure in the vicinity of the ,arctic sea-ice margin. J. Geophys. Res., 84: 1155-1164.

Perkins, H. (1970) Inertial oscillations in the Mediterranean. Massachusetts Institute of Technology - Woods Hole Oceanographic Institute, Ph.D. thesis, 155 p.

Pollard, R. T. and R. C. Millard, Jr. (1970) Comparison between observed and simulated wind-generated inertial oscillations. Deep-sea Res., 17: 813-821.

Pollard, R. T., P. B. Rhines, and R. O. R. Y. Thompson (1973) The deepening of the wind mixed layer. Geophys. Fluid Dyn., 3: 381-404.

Reed, R. J. and W. J. Campbell (1962) The equilibrium drift of the Ice Station Alpha. J. Geophys. Res., 67: 281-297.

Rossby, C.-G. (1932) A generalization of the theory of the mixing length with application to atmospheric and oceanic turbulence, Mass. Inst. Tech. Met. Pap. (4).

Rossby, C. G. (1938) On the mutual adjustment of pressure and velocity distribution in certain simple current systems, II. J. Mar. Res., 1: 239-263.

Rossby, C. G. and R. B. Montgomery (1935) The layer of frictional influence in wind and water current. Pap. Phys. Oceanogr. Met. Mass. Inst. Tech. Woods Hole Oceanogr. Inst., 3: 1-100.

Rothrock, D. A. (1975) The steady drift of an incompressible arctic ice cover. J. Geophys. Res., 80: 387-397.

Shuleikin, V. V. (1938) The drift of ice fields. Compt. Rend. (Doklady) Acad. Sci., URS, 19: 589-594.

Stern, M. E. (1975) Ocean Circulation Physics. Academic Press, New York, 246 p.

Tennekes, H. and J. L. Lumley (1972) A First Course in Turbulence. MIT Press, Cambridge, Mass., 300 p.

Wyngaard, J. C., O. R. Coté and K. S. Rao (1974) Modeling the atmospheric boundary layer. In Advances in Geophysics, 18A, Academic Press, New York, p. 193-212.

Zilitinkevich, S. S. (1975) Resistance laws and prediction equations for the depth of the planetary boundary layer. J. Atmos. Sci., 32: 741-752.